

---

# **Molecules in strong laser fields:**

## **Alignment and high-order harmonic generation**

---

**Christian Bruun Madsen**

Department of Physics and Astronomy  
University of Aarhus

**Progress report**

· May 2008 ·





---

# Contents

<b>Preface</b>	<b>ii</b>
<b>1 Introduction</b>	<b>1</b>
<b>2 Controlling the nuclear degrees of freedom by laser induced alignment</b>	<b>3</b>
2.1 The principle of laser induced alignment . . . . .	3
2.2 A semi-classical theory on laser control of internal molecular motion . . . . .	4
2.2.1 Modeling the molecule . . . . .	5
2.2.2 Field induced dynamics . . . . .	8
2.3 Results . . . . .	10
2.3.1 Simulating the Femtolab experiment . . . . .	10
2.3.2 Towards de-racemization . . . . .	11
<b>3 High-order harmonic generation from molecules</b>	<b>13</b>
3.1 The basics of high-order harmonic generation . . . . .	13
3.2 The single molecule spectrum with frozen degrees of freedom . . . . .	14
3.3 The photon picture and even versus odd harmonics . . . . .	16
3.4 Propagation of the molecular state . . . . .	18
3.4.1 Propagation of the rotational state . . . . .	18
3.4.2 Propagation of the electronic and vibrational state . . . . .	18
3.4.3 The effect of vibration . . . . .	20
3.4.4 Calculating the dipole . . . . .	21
3.5 Results . . . . .	23
3.5.1 High-order harmonic generation from alkanes . . . . .	23
3.5.2 Generation of even harmonics from the CO molecule . . . . .	27
3.6 Discussion of gauges and forms . . . . .	27
<b>4 Conclusion and outlook</b>	<b>29</b>
<b>Bibliography</b>	<b>31</b>



---

# Preface

This progress report accounts for my activities during the first half of my Ph.D. studies at the Department of Physics and Astronomy at the University of Aarhus.

My work falls into two parts. The past year, much effort has been put into understanding, simulating and elaborating on the Femtolab experiment described in Chapter 2. This is work in progress, although several important results have already been accomplished. Concurrently, I have been involved in the simulation of a separate Femtolab experiment on the multiphoton electron angular distribution from laser aligned CS<sub>2</sub> molecules, an issue treated in the publication [1]. It will not be addressed here. The rest of part A has been devoted to the studies of high-order harmonic generation from molecules. This work is outlined in Chapter 3. It has resulted in the three papers [2–4].

The reason for excluding some material and presenting the rest in reverse chronological order is to make the report as coherent and pedagogical as possible.

## Notational conventions

Atomic units,  $m_e = e = a_0 = \hbar = 1$ , are used throughout unless indicated otherwise.

## Acknowledgements

First of all, I would like to thank my supervisor Lars Bojer Madsen. His overview of the field of strong-field physics and his understanding of even the small details have been invaluable resources for me. I have also benefitted from discussions with several former and present colleagues at the Lundbeck Foundation Theoretical Center for Quantum System Research. Finally, I thank the Femtolab, and especially Henrik Stapelfeldt, for a very exciting and rewarding collaboration.

Christian Bruun Madsen

May 2008

---

# Introduction

This progress report deals with a number of non-perturbative responses of small molecules to strong laser fields. Even in the absence of the fields molecules are much more complex than atoms as they possess both electronic and nuclear degrees of freedom. The huge difference in the mass of the electron and that of the nuclei implies, however, that the time scales of electron and nuclear motion differ by orders of magnitude. The nuclei typically need femtoseconds or picoseconds to rearrange, whereas the characteristic time scale of the electron is the attosecond. Hence, the nuclear and electronic dynamics should be treated separately, and the quantum mechanical foundation of such approach is the Born-Oppenheimer (BO) approximation in which the wave function of the molecule splits into one part that comprises the rotation and vibrations of the nuclei and a part that describes the electronic state.

The division between the dynamics of the nuclei and the electrons is maintained when a laser field is applied in the sense that we can use laser fields with intensities of  $10^{12}$  to  $10^{13}$  W/cm<sup>2</sup> and durations ranging from picoseconds to nanoseconds to affect the nuclear degrees of freedom, with the electronic response entering only effectively as an induced dipole moment. The electrons, on the other hand, are addressed by laser fields with intensities of the order  $10^{14}$  W/cm<sup>2</sup> and durations of less than 100 femtoseconds. On that short a time scale the nuclear motion may be partly or completely disregarded.

Due to the high intensity, the average photon number is very large and the electromagnetic fields can be treated classically. Furthermore, the characteristic laser wavelength is the 800 nm produced by the titanium sapphire laser, and this length is large compared to the extension of the typical molecule of our interest. Because of this the spatial variation of the laser fields can safely be neglected, which amounts to the dipole approximation. Finally, we will use Coulomb gauge, and consequently our laser fields may be described by a vector potential  $\mathbf{A}(t)$  with the corresponding electric field  $\mathbf{F}(t) = -\partial\mathbf{A}(t)/\partial t$ .

In Chapter 2 it is demonstrated how lasers can be used to control the internal motion of a substituted biphenyl molecule. In particular, we present a semi-classical model that substantiates and generalizes an unprecedented Femtolab experiment demonstrating a significant change of the equilibrium angle between the two phenyl planes. The demonstrated angular control could open intriguing possibilities for ultrafast modulation and switching of electrical charge flowing through molecular junctions. Currently, we demon-

strate how to transfer a collection of molecules into one of the two mirror image forms, or enantiomers, a technique of general interest, as enantiomers often have very different effects, e.g., chemically, with the one being wanted and the other unwanted. Chapter 3 is about high-order harmonic generation, i.e., the production of high-frequency coherent radiation due to the direct electronic response to the laser field. This process has been the subject of extensive studies during the last couple of decades due to its possible applications, including the tomographic imaging of molecular orbitals and the generation of coherent ultraviolet attosecond pulses. Although high-order harmonic generation occurs for atoms as well as for molecules, studies of the process in the case of molecules are motivated by the expectation that the more degrees of freedom and non-spherical symmetry as compared to atoms may lead to richer physics and a higher degree of control. We shall in particular be concerned with the influence of frozen degrees of freedom on the emitted radiation. Finally, Chapter 4 provides a conclusion and an outlook.

---

## Controlling the nuclear degrees of freedom by laser induced alignment

In this chapter we will discuss how strong laser fields can be used to direct a molecule and parts of the molecule in space. The driving mechanism is that of laser induced alignment. We construct a semi-classical model that accounts for a pioneering experiment carried out by the Femtolab on the control of internal molecular motion. Finally, we demonstrate how a next generation of experiments can achieve controlled chiral symmetry breaking.

### 2.1 The principle of laser induced alignment

Laser induced alignment has been the subject of intense theoretical and experimental studies since the appearance of publications by Friedrich and Herschbach in the mid 90s (see, e.g., Ref. [5] for a review on the topic), and alone in this report we will make use of the technique repeatedly. Before proceeding to details, we want to specify, what we mean by alignment. If an order of molecules is created with respect to a space fixed axis, we speak of *alignment*. If further the inversion symmetry is broken, we speak of *orientation*. The concepts are illustrated in Fig. 2.1. To understand the laser-molecule interaction that makes a molecule align it is useful to start off from a macroscopic point of view. In general, when the molecule is exposed to an external electric field, not strong enough to ionize, the molecule is polarized and a dipole moment is induced. As the molecular structure is anisotropic, the molecule may polarize more readily in some directions than

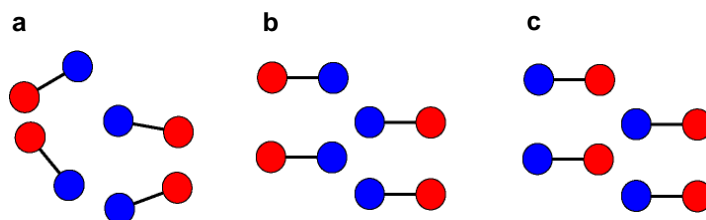


**Figure 2.1 | Alignment and orientation.** Illustrated with an ensemble of heteronuclear diatomic molecules. **a**, Unaligned. **b**, Aligned. **c**, Oriented.

others, and consequently the induced dipole moment need not be along the direction of the electric field, but is more generally related linearly to the applied electric field through the *polarizability tensor*.<sup>1</sup> Along with the permanent dipole, the induced dipole interacts with the external electric field and causes the molecule to rotate into a position that minimizes the energy of the dipole in the electric field. Now, the electric field of the laser is oscillating on a femtosecond time scale, whereas it will take picoseconds or more for the molecule to change its orientation, and therefore the interaction terms should be averaged over several laser cycles. This implies that the interaction of the field with the permanent dipole vanishes, as the electric field changes sign every half cycle. The polarizability, on the other hand, changes its sign along with the field, and therefore the interaction term containing the polarizability does not average out. As a result the alignment dynamics of the molecule in the laser field is determined by the polarizability.

In order to handle the alignment interaction on a microscopic level, the idea is to derive an effective description of the electronic response to the laser field. To this end we write the electric field of the laser as  $\mathbf{F}(t) = \mathbf{F}_0(t) \cos(\omega t)$ , where  $\mathbf{F}_0(t)$  encompasses the envelope and the polarization direction, and  $\omega$  denotes the laser frequency. We shall only be concerned with cases when the laser frequency is far off resonance with any energy levels of the molecule. Then a direct dipole coupling between molecular states is negligible and instead the dominant interaction is a Raman coupling of neighboring molecular eigenstates in the electronic ground state through the molecular levels of the excited electronic states. These latter electronic states can be adiabatically eliminated by integrating out their motion and introducing their influence as a polarizability tensor,  $\boldsymbol{\alpha}$ , to derive an effective interaction [6]

$$V_{\text{align}}(t) = -\frac{1}{4} \mathbf{F}_0^T(t) \boldsymbol{\alpha} \mathbf{F}_0(t), \quad (2.1)$$

which couples the nuclear states in the electronic ground state of the molecule. This interaction then leads to alignment by transferring an initial nuclear state with ill-defined angular confinement into an angularly confined superposition of molecular levels in the electronic ground state.

## 2.2 A semi-classical theory on laser control of internal molecular motion

With the alignment interaction (2.1) at hand we will launch into an exploration of a very recent experiment conducted by the Femtolab on the molecule 3,5-difluoro-3',5'-dibromobiphenyl (DFDBrBP), which is biphenyl with four of the hydrogens substituted by a pair of bromines (Br) and fluorines (F). The molecule is depicted in Fig. 2.2 on the next page.<sup>2</sup> In the experiments a gas of DFDBrBP molecules is exposed to a linearly polarized pulse with a duration of several nanoseconds, which is long compared to the time scale of the molecular rotation. This basically causes each molecule to align with the long axis, where the largest dipole moment is induced, along the polarization direction of the pulse. Meanwhile a linearly orthogonally polarized femtosecond pulse, referred to as the *kick*

---

<sup>1</sup>In principle, part of the induced dipole moment could depend nonlinearly on the electric field, but we shall not be concerned with the resulting higher order terms of the interaction, as they are typically negligible at the relevant field strengths.

<sup>2</sup>Note that from a theoretical point of view biphenyl would be just as interesting a molecule, but in the experiment the bromines and fluorines are needed to discriminate between the two rings of the molecule.

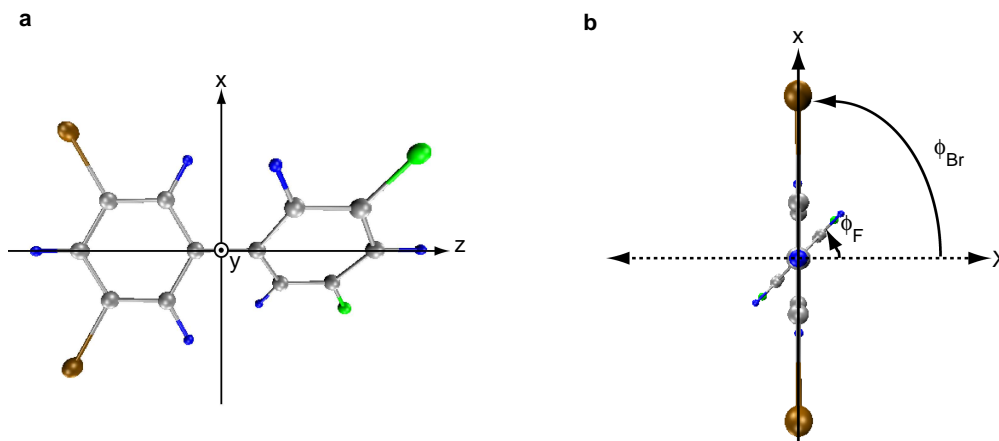


**Figure 2.2** | The molecule **3,5-difluoro-3',5'-dibromobiphenyl (DFDBrBP)**. The bromine and the fluorine atoms are indicated as brown and green, respectively. **a**, Side view of the molecule along with the molecular fixed (MF)  $xyz$  coordinate axes. The MF coordinates are chosen with the  $z$  axis pointing from the ring with the bromines towards the ring with the fluorines and the  $x$  axis coincides with the bromine ring. **b**, End view of the molecule. The bromine angle,  $\phi_{\text{Br}}$ , and fluorine angle,  $\phi_{\text{F}}$ , are measured from the LF  $X$  axis defined by the kick pulse polarization direction. (See Sec. 2.2.1 for details.)

*pulse*, is introduced and this will cause a three-dimensional alignment of the molecule a few picoseconds after the kick pulse, but more importantly it induces an internal motion of the two rings of the molecule.

One approach for modeling the experiment with DFDBrBP would be to describe the nuclear dynamics fully quantum mechanically. This is, however, a very ambitious approach, which is mastered only by one group world wide, the group of Tamar Seideman. Instead, we will resort to a semi-classical model, which, in addition to being easier on computational demands, accounts for the fundamental dynamics of the process and corroborates the experimental observations.

### 2.2.1 Modeling the molecule

To account for the motion of the nuclei, we will make use of two sets of coordinate systems: A *molecular fixed* (MF) frame attached to the molecule and a *laboratory fixed* (LF) frame specified by the lasers (see Fig. 2.2). The MF coordinates are chosen with the  $z$  axis pointing from the ring with the bromines towards the ring with the fluorines, and the  $x$  axis is chosen along the ring with the bromines.<sup>3</sup> The LF coordinates are chosen with the  $Z$  axis along the polarization direction of the long pulse and the  $X$  axis along the kick pulse polarization direction. Next, we simplify the situation by considering the two rings as rigid and lying with the long axis perfectly aligned along the  $Z$  axis. In this scenario we only need the two coordinates defining the angles of the rings with respect to the  $X$  axis to specify the configuration of the molecule.<sup>4</sup> Then in the absence of the kick pulse the task is reduced to describing the coupled rotations of the two rigid rings of the molecule

<sup>3</sup>We will use righthanded coordinate systems throughout this report.

<sup>4</sup>A normal mode analysis, carried out by Mikael Johansson from the Department of Chemistry at the University of Aarhus, has confirmed the validity of this simplification.

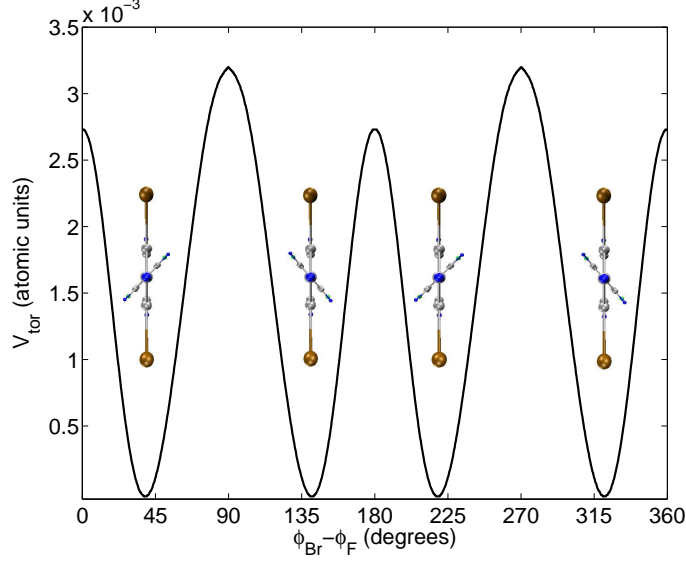


**Figure 2.3** | The torsional potential of DFDBrBP. Local maxima at angles corresponding to a coplanar and an orthogonal arrangement of the rings result in the twisted equilibrium shape of the molecule. The heights of the maxima can be varied by replacing the hydrogens at the ortho positions (next to the bond connecting the two rings) by other atoms or groups [7].

as given in the LF frame by the Hamiltonian

$$H_{\text{mol}} = -\frac{1}{2I_{\text{Br}}}\frac{\partial^2}{\partial\phi_{\text{Br}}^2} - \frac{1}{2I_{\text{F}}}\frac{\partial^2}{\partial\phi_{\text{F}}^2} + V_{\text{tor}}(\phi_{\text{Br}} - \phi_{\text{F}}), \quad (2.2)$$

where  $\phi_i, i = \text{Br}, \text{F}$ , is the azimuthal angle of the  $i$  ring,  $I_i$  the moment of inertia for a rotation of the  $i$  ring around the long axis of the molecule ( $I_{\text{Br}} = 8911925$ ,  $I_{\text{F}} = 1864705$ ) and  $V_{\text{tor}}(\phi_{\text{Br}} - \phi_{\text{F}})$  is the torsional potential. The torsional potential is shown in Fig. 2.3. We note, in passing, that this potential is  $\pi$ -periodic.

Rather than dealing with the Hamiltonian of Eq. (2.2), we make a change of coordinates that will allow a separation of the variables. Introducing the *dihedral angle*  $\phi_d = \phi_{\text{Br}} - \phi_{\text{F}}$  between the two rings and the *weighted azimuthal angle*  $\Phi = (1 - \eta)\phi_{\text{Br}} + \eta\phi_{\text{F}}$ , characterizing the rotation of the molecule, with  $\eta = I_{\text{F}}/(I_{\text{F}} + I_{\text{Br}})$ , we obtain

$$H_{\text{mol}} = \left(-\frac{1}{2I}\frac{\partial^2}{\partial\Phi^2}\right) + \left(-\frac{1}{2I_{\text{rel}}}\frac{\partial^2}{\partial\phi_d^2} + V_{\text{tor}}(\phi_d)\right) = H_{\Phi} + H_{\phi_d}. \quad (2.3)$$

Here  $I = I_{\text{Br}} + I_{\text{F}}$  is the total moment of inertia for rotation of the molecule around the long axis and  $I_{\text{rel}} = I_{\text{Br}}I_{\text{F}}/I$  is a relative moment of inertia for the two rings. A full rotation of either ring leaves us with the same molecule, and hence lead to  $2\pi$ -periodic boundary conditions of the eigenfunctions of  $H_{\text{mol}}$  from Eq. (2.2), i.e.,  $\psi(\phi_{\text{Br}} + 2\pi m, \phi_{\text{F}} + 2\pi n) = \psi(\phi_{\text{Br}}, \phi_{\text{F}})$ , with  $m$  and  $n$  integers. We shall assume that this property translates directly to  $\Phi$  and  $\phi_d$ , so that we simply need to consider eigenfunctions  $\psi(\Phi, \phi_d) = \xi(\Phi)\chi(\phi_d)$  of Eq. (2.3) that separates into a rigid rotation of the molecule as described by the  $2\pi$ -periodic function  $\xi(\Phi)$  and an internal motion, which is governed by the torsional potential and is accounted for by the  $2\pi$ -periodic function  $\chi(\phi_d)$ .<sup>5</sup> This separation is physically motivated

<sup>5</sup>Rigorously, the bounds for  $\Phi$  depend on  $\phi_d$  [8].

## Modeling the molecule

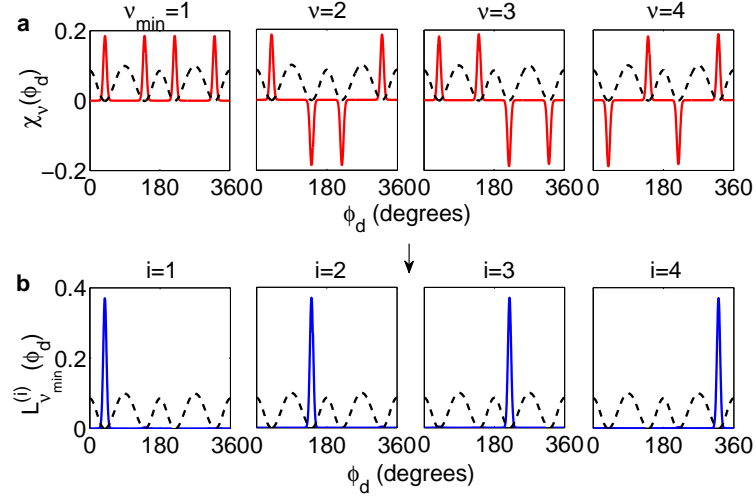


**Figure 2.4 | States of internal motion.** **a**, The four first (almost) degenerate energy eigenstates lying 1.71 meV above the minimum of the torsional potential. From linear combinations of these we obtain the corresponding four localized states shown in **b**. The torsional potential is indicated with a dashed line.

by considering the energy scales related to the rotation and the internal motion. The energy scale of the prior is given by  $\hbar^2/(2I) = 1.3 \mu\text{eV}$ . For the internal motion, on the other hand, the relevant energy is determined by the torsional potential, and a harmonic approximation of the potential near the minimum at  $39^\circ$  yields a frequency corresponding the energy 3.1 meV. If we then use that the period of motion is of the order Planck's constant divided by the energy, we see that the molecule will carry out an overall rotation, described by  $\Phi$ , on a nanosecond time scale while performing oscillations, characterized by  $\phi_d$ , of picosecond duration.

We will only treat the internal motion quantum mechanically, as the small energy separation of the rotational levels would call for the use of an unmanageably large number of rotational eigenfunctions in thermal equilibrium. The internal motion is described by the stationary Schrödinger equation

$$H_{\phi_d}|\chi_\nu\rangle = E_\nu|\chi_\nu\rangle, \quad (2.4)$$

with  $\nu = 1, 2, \dots$  denoting the energy eigenstates.<sup>6</sup> This equation is readily solved by first expanding the Hamiltonian onto a complete orthonormal basis of  $2\pi$ -periodic functions, truncated at some finite order, and next carrying out the diagonalization of the obtained matrix to get the eigenstates of the internal motion along with their energies. For the states below the torsional barriers there is an almost exact fourfold degeneracy, and this implies that linear combinations of the approximately degenerate states will also be stable at the time scales considered in the experiment. By forming appropriate linear combinations of such degenerate states, we obtain four solutions that are localized in the wells of the torsional potential. We will denote these states by  $|L_{\nu_{\min}}^{(i)}\rangle$ , with  $i = 1, 2, 3, 4$  and  $\nu_{\min}$  the smallest  $\nu$  among the four degenerate states. In Fig. 2.4 we show the four first energy eigenstates and the corresponding localized states. In the experiment the state of the molecule at time  $t_0$  prior to any pulses will not necessarily be either  $|L_1^{(1)}\rangle$  or  $|\chi_{100}\rangle$  or

<sup>6</sup>Note that due to the periodic boundary conditions, even the states with energies above the highest torsional barrier will be discrete rather than forming a continuum.

**Table 2.1** | The table lists the relevant polarizability components,  $\alpha_{ij}$ , of DFDBrBP in the MF frame as a function of the dihedral angle,  $\phi_d$ . The components are  $\pi$ -periodic with  $\alpha_{xx}(\phi_d) = \alpha_{xx}(\pi - \phi_d)$ ,  $\alpha_{yy}(\phi_d) = \alpha_{yy}(\pi - \phi_d)$  and  $\alpha_{xy}(\phi_d) = -\alpha_{xy}(\pi - \phi_d)$ . Also,  $\alpha_{yx} = \alpha_{xy}$ .

$\phi_d$ (degrees)		0	15	30	45	60	75	90
$\alpha_{xx}$ (atomic units)		217.694	215.590	209.463	200.975	192.431	186.240	184.048
$\alpha_{yy}$ (atomic units)		92.352	95.201	102.634	112.658	122.693	130.015	132.639
$\alpha_{xy}$ (atomic units)		0.000	-9.488	-16.360	-18.810	-16.225	-9.295	0.000

one of the other possibilities. Rather, the experiment is generally carried out on a gas of molecules, where the fraction  $P_1^{(1)}$  of the molecules is in state  $|L_1^{(1)}\rangle$  and the fraction  $P_{100}$  of the molecules is in state  $|\chi_{100}\rangle$ . This type of *mixed state* can be handled formally using the *density operator* [9]

$$\rho(t_0) = \sum_{\nu_{\min}} \sum_{i=1}^4 P_{\nu_{\min}}^{(i)} |L_{\nu_{\min}}^{(i)}\rangle \langle L_{\nu_{\min}}^{(i)}| + \sum_{\nu} P_{\nu} |\chi_{\nu}\rangle \langle \chi_{\nu}|, \quad (2.5)$$

with the  $P$ 's being weight factors that sum to unity, and where the latter sum includes the states above the torsional barrier. In the next section we will see, how to calculate expectation values using the density matrix.

We have now accounted for the internal motion of the molecule prior to the kick pulse. As to the corresponding classical rotation, we will make the simplest possible assumption, namely that the  $\Phi$  coordinate of the molecule is fixed at some constant value  $\Phi_0$ .

### 2.2.2 Field induced dynamics

We now turn to the part of the motion induced by the kick pulse. This motion is governed by the interaction potential of Eq. (2.1). By definition  $\mathbf{F}(t) = F_0(t)\hat{\mathbf{X}}$  for the kick pulse, and we use a Gaussian envelope  $F_0(t) = F_0 \exp\{-\ln(2)[t/(\tau_{\text{FWHM}}/2)]^2/2\}$  corresponding to a *full width at half maximum* (FWHM) of  $\tau_{\text{FWHM}}$ . As for the polarizability tensor it has been calculated by Mikael Johansson in the MF frame as a function of the dihedral angle (see Table 2.1) and must then be transformed into the LF frame by the application of directional cosine matrices [10]. We then arrive at the interaction

$$V_{\text{kick}}(\Phi, \phi_d, t) = -\frac{1}{4}F_0^2(t)[\alpha_{xx}(\phi_d)\cos^2(\Phi + \eta\phi_d) + \alpha_{yy}(\phi_d)\sin^2(\Phi + \eta\phi_d) - 2\alpha_{xy}(\phi_d)\cos(\Phi + \eta\phi_d)\sin(\Phi + \eta\phi_d)]. \quad (2.6)$$

For the succeeding analysis it will be helpful to note a few qualitative features of the potential. The potential is minimal for a fixed dihedral angle, if the two rings lie on either side of the  $X$  axis with the Br ring at the smaller angle ( $11^\circ$  at a dihedral angle of  $39^\circ$ ). We will denote this by the  $\parallel$ -geometry. Conversely, the potential is maximal if the molecule is rotated  $90^\circ$  from the  $\parallel$ -geometry, and we will denote this by the  $\perp$ -geometry. The two geometries are illustrated in Fig. 2.5. Next, in the  $\parallel$ -geometry the potential favors a reduction of the dihedral angle, whereas an increase of the dihedral angle is resulting from the  $\perp$ -geometry. Hence, the overall effect of the kick pulse will be to align the molecules into the  $\parallel$ -geometry and induce a motion of the dihedral angle.

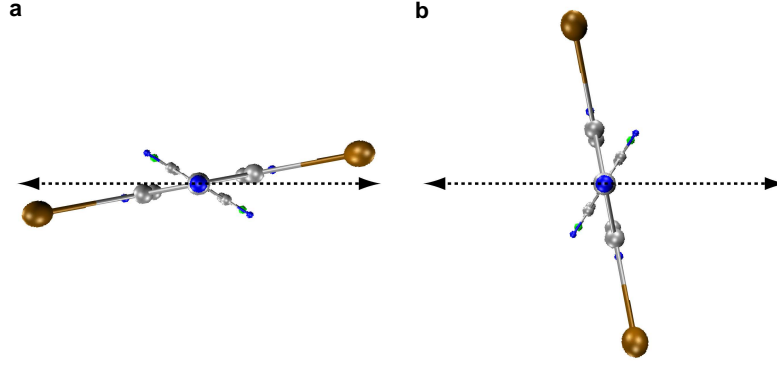


**Figure 2.5 | Kick pulse geometries.** The kick pulse polarization direction is indicated by the double arrow. **a**, The  $\parallel$ -geometry. **b**, The  $\perp$ -geometry.

With the above remarks in the back of our minds we then proceed with the quantitative analysis of the field induced dynamics. The state  $|\chi_\nu\rangle$  is no longer an eigenstate of the internal motion when the kick pulse is applied, but will develop into a superposition

$$|\chi_\nu\rangle \rightarrow |\chi_\nu^\Phi(t)\rangle = \sum_{\nu'} c_{\nu'}^\Phi(t) e^{-iE_{\nu'}(t-t_0)} |\chi_{\nu'}\rangle \quad (2.7)$$

with the coefficients determined by

$$\dot{c}_{\nu'}^\Phi(t) = -i \sum_{\nu} c_{\nu}^\Phi(t) e^{-i(E_{\nu} - E_{\nu'})(t-t_0)} \langle \chi_{\nu'} | V_{\text{kick}}(\Phi, t) | \chi_{\nu} \rangle, \quad (2.8)$$

as is readily verified from the time-dependent Schrödinger equation. Once these new states of internal motion have been determined, the expectation value of any operator  $O$  can be found by tracing the product of the density matrix with the operator, i.e.,  $\langle O(t) \rangle = \text{Trace}[\rho(t)O]$ . In particular, we shall need the expectation value of the dihedral angle and of the kick potential from Eq. (2.6). From the latter we obtain the torque, which causes the molecule to swing into the  $\parallel$ -geometry. If the molecule lies at an angle  $\Phi$  it will be exposed to a torque  $-\partial \langle V_{\text{kick}}(\Phi, t) \rangle / \partial \Phi$  directed along the  $Z$  axis and will hence achieve an angular acceleration given by

$$I\ddot{\Phi} = -\frac{\partial \langle V_{\text{kick}}(\Phi, t) \rangle}{\partial \Phi}. \quad (2.9)$$

Together with the initial conditions given at the end of Sec. 2.2.1, Eqs. (2.8) and (2.9) provide a coupled set of differential equations that may be integrated to obtain the coordinates  $\Phi(t)$  and  $\langle \phi_d(t) \rangle$  at time  $t$ . Rather than solving these coupled equations, we will assume that the angle  $\Phi$  has the constant value  $\Phi_0$  during the short time interval of the kick pulse, and we integrate Eq. (2.9) twice to arrive at

$$\Phi(t) = \Phi_0 - t \frac{1}{I} \left( \frac{\partial}{\partial \Phi} \int_{\infty}^{\infty} dt' \langle V_{\text{kick}}(\Phi, t') \rangle \right) \Big|_{\Phi=\Phi_0}. \quad (2.10)$$

Consistently, Eq. (2.8) is solved with  $\Phi$  frozen at  $\Phi_0$ .

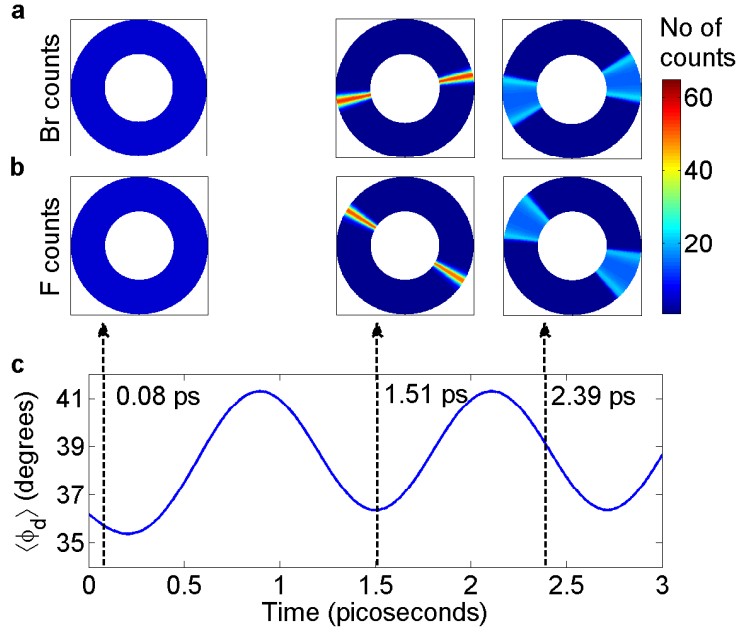


**Figure 2.6 | Simulation of the Femtolab experiment.** The kick pulse is polarized along the horizontal direction with intensity  $5 \times 10^{12}$  W/cm<sup>2</sup> and FWHM of 700 fs. **a**, The angular distribution of the Br ring at three different times (0.08 ps, 1.51 ps and 2.39 ps). **b**, The angular distribution of the F ring at the same three instants. **c**, The expectation value of the dihedral angle for a molecule starting out in the  $\parallel$ -geometry (defined in Fig. 2.5 on the preceding page).

## 2.3 Results

### 2.3.1 Simulating the Femtolab experiment

Having developed the theoretical model, we are now in a position to simulate the gas of molecules given in the experiment. The gas is realized, in the computer, by picking a number of uniformly distributed initial values for  $\Phi_0$  in the interval  $[0, 2\pi]$  along with an initial density matrix,  $\rho(t_0)$ . We have assumed that  $\rho(t_0) = |L_1^{(1)}\rangle\langle L_1^{(1)}|$ , corresponding to a rotationally cold gas of molecules with an initial dihedral angle  $\langle \phi_d \rangle_i = 39^\circ$ . We then propagate each of these realizations according to Eqs. (2.8) and (2.10), and this yields an ensemble of  $\Phi(t)$ 's and  $\langle \phi_d(t) \rangle$ 's from which we can produce output similar to the experimental observations. Figure 2.6 shows the results of a calculation using a kick pulse of intensity  $5 \times 10^{12}$  W/cm<sup>2</sup> and FWHM of 700 fs, chosen to match the parameters of the experiment. The two panels a and b illustrate the angular distribution of bromines and fluorines at three instants, calculated from the relations  $\phi_{\text{Br}}(t) = \Phi(t) + \eta\langle \phi_d(t) \rangle$  and  $\phi_{\text{F}}(t) = \Phi(t) - (1 - \eta)\langle \phi_d(t) \rangle$ . These plots can be directly compared to the experiment, where the angular distributions are detected by Coulomb exploding the molecule and recording the directions of the produced ion fragments. The theoretical results show good agreement with the experimental observations: From having an almost uniform angular distribution of the molecules, the kick pulse forces the molecules towards the  $\parallel$ -geometry resulting in a maximal angular confinement 1.3 ps after the peak of the kick pulse, followed by a spreading of the molecules. In the experiment the maximal alignment is reached some time between 1.5 and 3.5 ps. Next, we consider the induced dihedral dynamics, and we concentrate on a molecule starting out in the  $\parallel$ -geometry. Panel c shows how  $\langle \phi_d(t) \rangle$

exerts an oscillating behavior once the kick pulse is over, and the period of 1.21 ps simply stems from interference of first localized state with the corresponding localized state lying 3.42 meV above. No further energy levels are populated appreciably at the kick strength (intensity and duration) used in the experiment. At the time of writing the experimental observations are still being analyzed, but the data seems to be consistent with these oscillations even at a quantitative level.

### 2.3.2 Towards de-racemization

The previous theoretical results along with the experiment show that control of the internal motion of molecules can in fact be obtained by laser induced alignment. The ability to modify the dihedral angle, also denoted *torsional alignment*, was recently addressed elsewhere and a broad range of potential applications, including charge transfer and molecular junctions, was proposed [11]. Here we will focus on another application, where we do not only wish to modify the dihedral angle, but overcome the torsional barrier in a selective way.

When DFDBrBP is produced it is a *racemic mixture*, i.e., it is composed of equal numbers of molecules with the Br ring tilted  $39^\circ$  with respect to the F ring and with the Br ring tilted  $-39^\circ$  with respect to the F ring. As the two versions of the molecule cannot be made to overlap by means of rotation the molecule is chiral, and the two species are known as different *enantiomers*. The *R enantiomer* is made up of states  $|L_\nu^{(1,3)}\rangle$  and the *S enantiomer* of states  $|L_\nu^{(2,4)}\rangle$  (c.f. Figs. 2.3 and 2.4).<sup>7</sup> Chemically and biologically the effects of enantiomers can differ dramatically and the production of compounds consisting of only the one kind is of immense industrial interest [12]. Our goal is to convert a racemic mixture into a sample of one type of enantiomers only, a process known as *de-racemization*. To this end we note that a repetition of the experiment, but with increased kick strength, will allow us to overcome the torsional barrier and transfer population from, say,  $|L_\nu^{(3)}\rangle$  to  $|L_\nu^{(2)}\rangle$ . This is, however, not the end of the story. As the molecules are fixed with the long axis along the LF  $Z$  axis by alignment, molecules with the Br ring pointing in the positive and in the negative  $Z$  direction both occur (cf. Fig. 2.1 on page 3). This poses a problem, because the R enantiomer pointing with the long axis in one direction has the same  $XY$  projection as the S enantiomer pointing in the opposite direction and the kick pulse interaction is only susceptible to this projection [cf. Eq. (2.6)]. Consequently, as we convert R into S enantiomers, an equal number of molecules starting out as S enantiomers will be converted simultaneously into R enantiomers and altogether no de-racemization takes place.<sup>8</sup> To overcome this problem we introduce an interaction, e.g., an electrostatic field, that orients the long axis of the molecule. This makes the projection of the enantiomers onto the  $XY$  plane unambiguous, and the alignment interaction is able to discriminate the different enantiomers. If we then additionally fix the initial Br (or F) angle at a proper value by a long alignment pulse, the introduction of the (horizontally polarized) kick pulse leads to de-racemization. This is illustrated in Fig. 2.7. Note that we have reduced the torsional barriers with a factor of four rather than increasing the kick strength to some unrealistic value that would lead to a destruction of the molecules.

<sup>7</sup>In what follows, we shall only consider the localized states  $|L_\nu^{(2)}\rangle$  and  $|L_\nu^{(3)}\rangle$ , as all results on  $|L_\nu^{(2)}\rangle$  ( $|L_\nu^{(3)}\rangle$ ) can be applied directly to  $|L_\nu^{(4)}\rangle$  ( $|L_\nu^{(1)}\rangle$ ).

<sup>8</sup>Mathematically, the problem of the alignment interaction is that it is invariant under inversion of the molecular coordinates. No such invariant interaction can on its own lead to de-racemization [13].

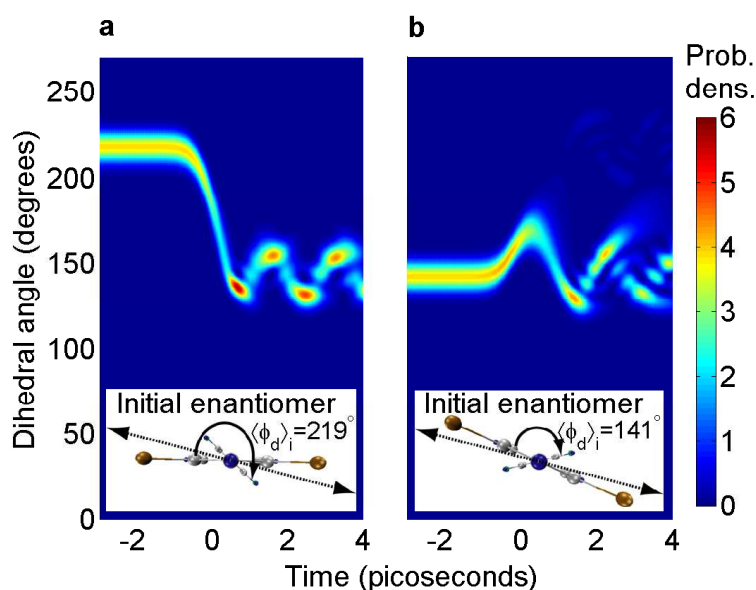


**Figure 2.7 | De-racemization by orientation and field induced alignment.** Orientation ensures that the Br rings point out of the plane of the paper and the alignment (double arrow) fixes the initial Br (or F) angle. Dihedral dynamics is then initiated by a kick pulse of horizontal polarization and with intensity  $1.2 \times 10^{13}$  W/cm<sup>2</sup> and FWHM of 1.0 ps. The time evolution of molecules starting out with a dihedral angle of 219° and 141° is shown in **a** and **b**, respectively.

Such modification of the torsional potential may be accomplished by substitution of the hydrogens at the ortho positions (cf. Fig. 2.3 on page 6). The effect of the kick pulse is clearly to create an excess of S enantiomers. To quantify the efficiency of the process we integrate the probability density in the interval  $[90^\circ, 180^\circ]$  to get the fraction of S enantiomers and the interval  $[180^\circ, 270^\circ]$  to get the fraction of R enantiomers. This shows that after the pulse 99% of the molecules starting out as R has changed into S enantiomers, whereas only 13% of the molecules starting out as S has changed into R enantiomers. We end by noting that the efficiency may be improved by using multiple kick pulses (at different polarization directions and delays) and that the inverse process, i.e., causing an excess of R enantiomers, is simply achieved by inverting the orientation of the molecules.

---

## High-order harmonic generation from molecules

In this chapter we treat high-order harmonic generation from molecules. The phenomenon is accounted for by solving the time-dependent Schrödinger equation, and we first discuss, how to retrieve the observable, the harmonic spectrum, from such solution. We then go on to develop a method for handling frozen degrees of freedom, and when combined with the strong-field approximation, this will enable us to calculate harmonic spectra from even polyatomic molecules such as the alkanes.

### 3.1 The basics of high-order harmonic generation

The exploitation of a nonlinear medium for second harmonic generation, i.e., frequency doubling of laser radiation, is practically as old as the operating laser itself. With the availability of femtosecond lasers in the late 80s, with typical intensities between  $10^{14}$  and  $10^{15}$  W/cm<sup>2</sup>, a new type of frequency conversion was observed [14], viz., when a gas of atoms is exposed to such fields, it emits not only second or third order harmonics, but a *high-order harmonic generation* (HHG) takes place, where the atoms coherently emit radiation at high-order harmonics of the laser frequency with an almost constant efficiency until some cutoff. Molecules exhibit the same kind of behavior. In this case, however, nuclear structure and dynamics will affect the radiative response.

Basically, the harmonic radiation comes about, because the interaction of the molecule with a strong laser field induces a time varying molecular dipole. The fact that the electric field of a typical harmonic-generating laser exerts a force on the electrons nearly as great as the forces between the nuclei and the bound electrons implies that the interaction is non-perturbative, and the dipole must be worked out by solving the time-dependent Schrödinger equation

$$i\partial_t|\Psi(t)\rangle = [H_0 + V_{\text{HHG}}(t)]|\Psi(t)\rangle. \quad (3.1)$$

Here  $H_0 = T_N + T_e + V_C$  is the field-free molecular Hamiltonian consisting of the kinetic energy of the nuclei and the electrons along with the Coulomb potential, which describes the attraction and repulsion of the charged particles. Finally, the *length gauge* dipole interaction term is given by  $V_{\text{HHG}}(t) = \sum_n \mathbf{F}(t) \cdot \mathbf{r}_n$  and couples the electric field,  $\mathbf{F}(t)$ , of harmonic-generating laser to the displacements,  $\mathbf{r}_n$ , of the electrons. With the solution

of Eq. (3.1) at hand, we can calculate the induced molecular dipole at any time from the expectation value of the electronic dipole operator,  $\mathbf{d}$ .<sup>1</sup> The corresponding *harmonic spectrum* of radiation of polarization  $\mathbf{e}$  is then obtained from the Fourier transform of the dipole acceleration [15], i.e.,

$$S_e(\omega_{\text{HHG}}) \propto |A_e(\omega_{\text{HHG}})|^2, \quad \text{with} \quad A_e(\omega_{\text{HHG}}) = \mathbf{e} \cdot \int dt e^{i\omega_{\text{HHG}}t} \frac{d^2}{dt^2} \langle \mathbf{d}(t) \rangle, \quad (3.2)$$

where  $\langle \mathbf{d}(t) \rangle$  is the expectation value of the induced molecular dipole. The time integration is carried out over the pulse length of the harmonic-generating laser. Before proceeding, we make some points concerning the fact that experiments deal with a gas of molecules rather than a single molecule. First, the spectrum of a gas should be calculated from the dipole correlation function, rather than the expectation value of the induced dipole. For a large gas of uncorrelated molecules this, however, amounts to the same thing [16]. Second, the radiation emitted from one molecule has to propagate through the gas of the remaining molecules. Understanding the single-molecule response is, nonetheless, a prerequisite for understanding the more complex situation involving all of the molecules.

## 3.2 The single molecule spectrum with frozen degrees of freedom

The typical experiment on HHG from molecules consists of a preparation of a molecular gas by a number of alignment pump pulses, followed by a short strong laser pulse that drives the HHG [17, 18] (see Fig. 3.1 on the next page). In this type of setup the rotation of the molecule is practically frozen during the interaction with the harmonic-generating laser. Besides having a frozen rotation, it is usually assumed that the laser field will only interact with a single electron from the *highest occupied molecular orbital* (HOMO) whereas all the other electrons remain frozen. This is the *single-active-electron* (SAE) approximation, and it greatly simplifies the solution of Eq. (3.1). We shall follow the approach, although many-electron effects may yield important contributions to the harmonic radiation [19].

To proceed, we need to consider a representative molecule of the gas prior to any pump and driving pulses. First, the rotational states are often very close in energy (cf. Chapter 2) and even at low temperatures the molecule is likely to be in an excited rotational state. Second, typically more electrons from the molecule can contribute significantly to the HHG because of degeneracy of the molecular orbitals. We therefore treat the initial state as a mixed state, a stationary thermal state at temperature  $T$ , and this is done using the density operator<sup>2</sup>  $\rho_0 = \exp(-H_0/k_B T) / \text{Trace}[\exp(-H_0/k_B T)]$ , with  $k_B$  Boltzmann's constant. We want to resolve the molecular initial state on energy eigenstates, and according to the BO approximation, we can separate the electron and nuclear motion. We will assume that only the electronic ground state is populated, and we introduce an index  $\lambda$  in order to be able to discriminate between the degenerate HOMOs of the active electron. By neglecting the rotational-vibrational coupling, the BO nuclear wave function is split into a rotational part and a vibrational part. The rotation is characterized by the total orbital angular momentum,  $J$ , the asymmetric top quantum number,

<sup>1</sup>The huge difference between electron and nuclear masses implies that the displacements of the nuclei will be less significant and consequently that the nuclear dipole terms can safely be neglected.

<sup>2</sup>The density operator was introduced on page 8.

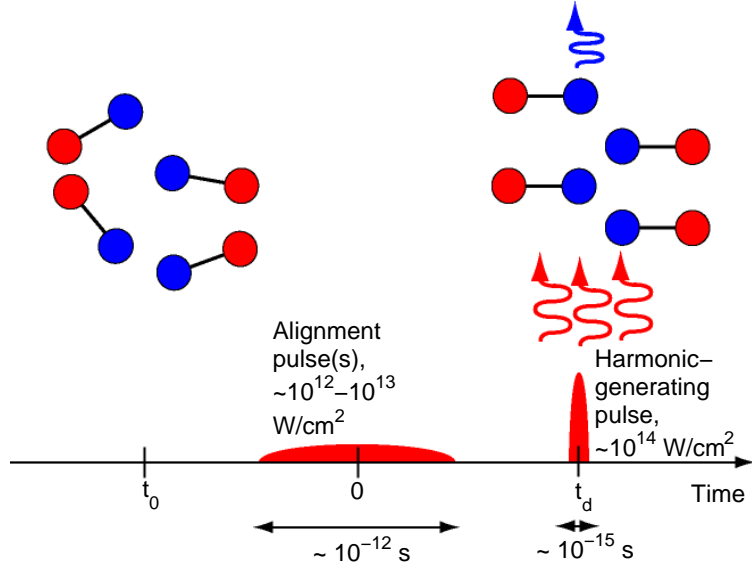


**Figure 3.1 | Typical experiment on HHG from molecules.** An initially thermal distribution of molecules is prepared by alignment and harmonics are generated at time  $t_d$  with respect to the alignment pulse(s).

$\tau$ , and the magnetic quantum number,  $M$ . We shall assume that only the vibrational ground state,  $|\chi_0\rangle$ , is occupied. All things considered, we may specify the molecular energy eigenstates by  $|\psi_\lambda\chi_0\Phi_{J\tau M}\rangle$ . Each of these field-free eigenstates develop from time  $t_0$  prior to any laser pulses to time  $t$  according to the *time evolution operator*,  $\mathcal{U}(t, t_0)$ , i.e.,  $|\psi_\lambda\chi_0\Phi_{J\tau M}(t)\rangle = \mathcal{U}(t, t_0)|\psi_\lambda\chi_0\Phi_{J\tau M}\rangle$ , where the time evolution operator itself is unitary and satisfies the full Schrödinger equation that encompasses any number of orienting pump pulses followed by the short, intense laser pulse that drives the HHG [9]. The usual orientation pulses are not strong enough to affect the vibrational or electronic motion appreciably, while we recall that the rotation can be considered as frozen during the short harmonic-generating pulse. Thus, if the delay between the first orienting pulse and the driving pulse is denoted by  $t_d$ , we can split the time evolution operator according to  $\mathcal{U}(t, t_0) \simeq \mathcal{U}_{\text{HHG}}(t, t_0) \otimes \mathcal{U}_{\text{orient}}(t_d, t_0)$  for a description of the evolution when the HHG is produced, where  $\mathcal{U}_{\text{HHG}}(t, t_0)$  propagates the electronic and vibrational part of the molecular state during the pulse of the driving laser and  $\mathcal{U}_{\text{orient}}(t_d, t_0)$  accounts for the rotational state of the molecule. The initial energy eigenstates then evolve as follows

$$|\Psi_{J\tau M}^\lambda(t)\rangle \simeq (\mathcal{U}_{\text{HHG}}(t, t_0)|\psi_\lambda\chi_0\rangle) \otimes (\mathcal{U}_{\text{orient}}(t_d, t_0)|\Phi_{J\tau M}\rangle) = |\psi_\lambda\chi_0(t)\Phi_{J\tau M}(t_d)\rangle. \quad (3.3)$$

We return to the propagation of the molecular state in Sec. 3.4 on page 18. Our present goal is to unravel the dependence of the harmonic spectrum on the frozen molecular degrees of freedom. According to Eq. (3.2) we must then find the expectation value of the dipole operator. To this end we introduce the position basis,  $|\mathcal{R}\mathcal{Q}\mathbf{r}\rangle$ . Here the *Euler angles*,  $\mathcal{R} = (\phi, \theta, \chi)$ , describe the rotation of the molecule with respect to the LF frame. Following the conventions of Zare [10]  $\theta$  is the angle between the  $z$  axis in the MF frame and the  $Z$  axis in the LF frame,  $\phi$  denotes a rotation around the  $Z$  axis, and finally  $\chi$  denotes a rotation around the  $z$  axis (cf. Sec. 2.2.1 on page 5 for an introduction to MF and LF frames). The vibrational coordinates,  $\mathcal{Q} = (q_1, q_2, \dots, q_m)$ , characterize

internal displacements of the nuclei and  $\mathbf{r} = \mathbf{r}_n$  is the coordinate of the active electron. In the position basis the dipole operator is simply proportional to the sum of electron displacements and<sup>3</sup>

$$\begin{aligned} \langle \mathbf{d}(t) \rangle &= \text{Trace} \left[ U(t) \rho_0 U^\dagger(t) \mathbf{d} \right] \\ &= \int d\mathcal{R} d\mathbf{Q} d\mathbf{r} \int d\mathcal{R}' d\mathbf{Q}' d\mathbf{r}' \langle \mathcal{R}' \mathbf{Q}' \mathbf{r}' | \left( \sum_{J\tau M\lambda} P_{J\tau} P_\lambda |\Psi_{J\tau M}^\lambda(t)\rangle \langle \Psi_{J\tau M}^\lambda(t)| \right) | \mathcal{R} \mathbf{Q} \mathbf{r} \rangle \\ &\quad \times \langle \mathcal{R} \mathbf{Q} \mathbf{r} | \mathbf{d} | \mathcal{R}' \mathbf{Q}' \mathbf{r}' \rangle \simeq \int d\mathcal{R} G_{td}(\mathcal{R}) \sum_\lambda P_\lambda \langle \mathbf{d}_\lambda(\mathcal{R}, t) \rangle, \end{aligned} \quad (3.4)$$

with  $P_\lambda$  the initial distribution of the degenerate electronic states,

$$\langle \mathbf{d}_\lambda(\mathcal{R}, t) \rangle = \int d\mathbf{Q} |\chi_0(\mathbf{Q}, t)|^2 \int d\mathbf{r} |\psi_\lambda(\mathcal{R}; \mathbf{Q}; \mathbf{r}, t)|^2 (-\mathbf{r}), \quad (3.5)$$

$$G_{td}(\mathcal{R}) = \sum_{J,\tau,M} P_{J\tau} |\Phi_{J\tau M}(\mathcal{R}; t_d)|^2, \quad (3.6)$$

and  $P_{J\tau} \propto \exp(-E_{J\tau}/k_B T)$  is the Boltzmann weight of the initial asymmetric top state  $|J\tau M\rangle$  of energy  $E_{J\tau}$ . (Also, note that  $\int d\mathcal{R} \rightarrow \int_0^{2\pi} d\phi \int_0^\pi d\theta \sin\theta \int_0^{2\pi} d\chi$ .) Inserting this into Eq. (3.2) we arrive at an expression for the harmonic spectrum

$$\begin{aligned} S_e(\omega_{\text{HHG}}) &\propto \left| \sum_\lambda P_\lambda \int d\mathcal{R} G_{td}(\mathcal{R}) A_e^\lambda(\omega_{\text{HHG}}, \mathcal{R}) \right|^2, \quad \text{with} \\ A_e^\lambda(\omega_{\text{HHG}}, \mathcal{R}) &= \mathbf{e} \cdot \int dt e^{i\omega_{\text{HHG}} t} \frac{d^2}{dt^2} \langle \mathbf{d}_\lambda(\mathcal{R}, t) \rangle. \end{aligned} \quad (3.7)$$

The essence of this result is the fact that to reproduce the experimental spectrum from the single molecule spectrum, when the frozen degrees of freedom occur, one cannot simply add the spectra stemming from each orientation and each HOMO. Instead, the dipoles should be added directly. Physically, this is due to the fact that the electric fields of the molecules add up rather than the intensities of these fields. Nevertheless, there are special cases when the degeneracy enters simply as a factor multiplying the signal from a single HOMO. For example consider the case when the HOMOs differ simply by a rotation. Then, if the molecules have not been prepared prior to the harmonic-generating pulse, we have an unaligned ensemble of molecules, i.e.,  $G_{td} = 1/(8\pi^2)$ , and it is obvious that the HOMOs must each give rise to the same complex number when the single HOMO amplitude,  $A_e^\lambda(\omega_{\text{HHG}}, \mathcal{R})$ , is averaged over all orientations. It then follows from Eq. (3.7) that the degeneracy will enter as a factor multiplying the signal from a single HOMO.

### 3.3 The photon picture and even versus odd harmonics

In terms of photons, HHG is understood as the absorption of a large number of photons from the harmonic-generating laser, followed by the emission of the absorbed energy in

<sup>3</sup>Speaking of *the* active electron may seem in conflict with the fact that the electrons of the molecule are identical particles. As the dipole operator, however, is a sum of single electron terms, we may replace an evaluation of the full dipole operator in the fully antisymmetrized electronic wave function by a single term of the determinant, and the electron integrals that do not include the dipole operator integrate to unity [20].

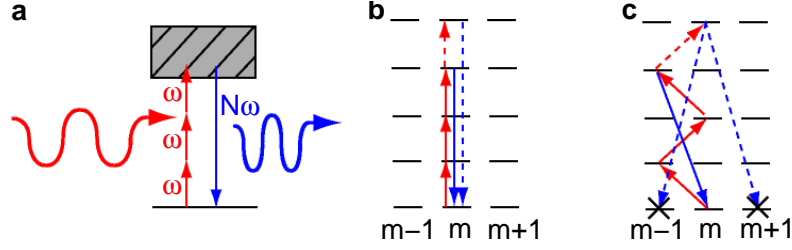


**Figure 3.2 | The photon picture.** **a**, A high-order harmonic results from the conversion of many laser photons into one. **b**, The dipole transitions for a linear molecule with the internuclear axis parallel to the polarization direction and with an initial electronic orbital angular momentum projection along the internuclear axis of  $m$ . **c**, The same as in **b**, but with the internuclear axis perpendicular to the polarization direction. In this case only an even number of dipole transitions may lead back to the initial state.

the form of one high-order harmonic photon. This is pictured in Fig. 3.2a. In particular, the photon picture allows us to understand the difference in generating harmonic photons of even and odd orders. To see this we first note that emission of a harmonic of order  $N$  comprises  $N+1$  dipole transitions, namely the  $N$  absorptions of a laser photon, and the emission of a single high-order harmonic photon. Let us then have a look at a diatomic molecule in a  $\Sigma$  ground state generating harmonic radiation polarized along the linear polarization direction of the harmonic-generating laser. We refer to Fig. 3.2b-c for a visualization of the arguments below. Consider first the case when the internuclear axis of the molecule is parallel to the driving laser so that only the component  $\hat{\parallel}$  of the dipole operator parallel to the internuclear axis is active (panel b). This component has a  $\Delta\Lambda = 0$  selection rule, with  $\Lambda$  the absolute value of the projection of the total electronic orbital angular momentum on the internuclear axis. Initially the molecule is in its  $\Sigma$  ground state and because of  $\Delta\Lambda = 0$  it stays in the manifold of  $\Sigma$  states. The  $\Sigma$  state, from which the final recombination step occurs, is hence accessible by the absorption of both an even and odd number of photons and, consequently, both even and odd harmonics may be produced. If the molecule is instead lying with the internuclear axis perpendicular to the polarization direction of the driving laser, only the component  $\hat{\perp}$  of the dipole operator perpendicular to the internuclear axis is active and this component has a  $\Delta\Lambda = \pm 1$  selection rule (panel c). Consequently, only odd harmonics are allowed since the  $\Pi$  state, from which the recombination occurs, can only be reached by the absorption of an odd number of photons. In the more general case, when the molecule is lying at an angle  $\theta$  with respect to the polarization axis of the driving laser, the situation is analyzed by using the transition operator  $O_N(\theta) = \prod_{i=1}^{N+1} (\hat{\parallel}_i \cos \theta + \hat{\perp}_i \sin \theta)$  corresponding to emission of a harmonic of order  $N$ . In the limits of parallel ( $\theta = 0^\circ$ ) and perpendicular ( $\theta = 90^\circ$ ) orientation we recover the results discussed above. If the molecule is not perfectly oriented, but rather characterized by some orientational distribution  $G_{t_d}(\mathcal{R})$ , we make a weighted average of  $O_N(\theta)$  corresponding to different orientations in accordance with the findings of the previous section [cf. Eq. (3.7)]. Of special interest is the case of an unaligned ensemble of molecules. Since  $G_{t_d} = 1/(8\pi^2)$  only the terms of  $O_N(\theta)$  with combinations of the cosines and sines yielding an even function on  $[0, \pi]$  will survive the averaging, i.e., the terms containing an even number of the  $\hat{\parallel}$  operator. From the selection rules it is, however, clear that the total number of  $\Lambda$  changing transition must be an even number and thus the total number of dipole transitions is even, implying that only odd harmonics are emitted in the unaligned case.

### 3.4 Propagation of the molecular state

We now know how to treat the frozen degrees of freedom and combined with the photon picture this enables us to predict the occurrence and absence of even harmonics. The objective of this section is to discuss, how the propagation of the molecular state, as prescribed by Eq. (3.3), is implemented in order to actually calculate harmonic spectra.

#### 3.4.1 Propagation of the rotational state

Propagation of the rotational part of the molecular state is obtained by solving the Schrödinger equation for the rotational degrees of freedom. For the general asymmetric top this is a challenging task, but for a linear molecule in a  $\Sigma$  electronic state the field-free rotational eigenfunctions reduce to spherical harmonics,  $Y_J^M(\theta, \phi)$ . In the case of a series of pump pulses, composed of a number of orienting electric fields  $F_{\text{orient}}^{(m)}(t)$  and alignment pulses with envelopes  $F_{\text{align},0}^{(n)}(t)$ , all of the same linear polarization direction, defining the LF  $Z$  axis, we must then simply solve the one-dimensional time-dependent Schrödinger equation given by the Hamiltonian

$$H_{\text{rot}} = B\hat{J}^2 - \mu \sum_m F_{\text{orient}}^{(m)}(t) \cos \theta - \frac{1}{4} \sum_n F_{\text{align},0}^{(n)2}(t) [\alpha_{\parallel} \cos^2 \theta + \alpha_{\perp} \sin^2 \theta], \quad (3.8)$$

where  $\hat{J}^2$  is the squared total orbital angular momentum operator,  $B$  is the rotational constant,  $\mu$  is the permanent dipole moment of the molecule and  $\alpha_{\parallel}$  and  $\alpha_{\perp}$  are the polarizability components along and perpendicular to the internuclear axis. The equation is solved by a procedure analogous to the one outlined for the internal motion of DFDBrBP (see Chapter 2), except that now the field-free states are known analytically and the matrix elements of  $H_{\text{rot}}$  can be worked out in hand [10].

#### 3.4.2 Propagation of the electronic and vibrational state

Next, we must propagate the electronic and vibrational part of the molecular state with the rotational degrees of freedom frozen, i.e., for a fixed orientation  $\mathcal{R}$  of the molecule. Because of the SAE approximation we introduce an effective field-free Hamiltonian, which involves only the active electron

$$H'_0 = T_N^{\text{vib}} + \mathbf{p}^2/2 + V_{\lambda}(\mathcal{R}; \mathbf{Q}; \mathbf{r}) \quad (3.9)$$

with  $T_N^{\text{vib}}$  being the vibrational part of the nuclear kinetic energy,  $\mathbf{p}^2/2$  the kinetic energy of the electron, and  $V_{\lambda}(\mathcal{R}; \mathbf{Q}; \mathbf{r})$  an effective, time-independent potential for the active electron owing to the nuclei and the remaining electrons. If we then let  $|\psi_{\lambda}\chi_0\rangle$  denote the field-free electronic and vibrational ground state, which satisfies  $H'_0|\psi_{\lambda}\chi_0\rangle = E_0|\psi_{\lambda}\chi_0\rangle$ , we can write down a formal solution of Eq. (3.9):

$$\begin{aligned} |\psi_{\lambda}\chi_0(t)\rangle &= \mathcal{U}_{\text{HHG}}(t, t_0)|\psi_{\lambda}\chi_0\rangle \\ &= \left[ e^{-iE_0(t-t_0)} + \int_{t_0}^t dt' G(t, t') V_{\text{HHG}}(t') e^{-iE_0(t'-t_0)} \right] |\psi_{\lambda}\chi_0\rangle. \end{aligned} \quad (3.10)$$

In the second equality time evolution is split into a part, which describes the trivial time evolution, as if no field was present, and a part, which accounts for the non-trivial time

evolution due to the presence of the laser field. The latter involves a so-called Green's function,  $G(t, t')$ , defined from the equation

$$[i\partial_t - H'_0 - V_{\text{HHG}}(t)] G(t, t') = \delta(t - t'). \quad (3.11)$$

It is easily verified directly that (3.10) is a solution to Eq. (3.9) by exploiting Eq. (3.11) and the fact that  $|\psi_{\lambda\chi_0}\rangle$  is an eigenstate of  $H'_0$ . To move on, we introduce the Lippmann-Schwinger equation

$$G(t, t') = G_0(t, t') + \int_{t'}^t dt_1 G_0(t, t_1) \Delta V G(t_1, t'). \quad (3.12)$$

Here  $\Delta V = V_{\lambda}(\mathbf{R}; \mathbf{Q}; \mathbf{r}) - V^+(\mathbf{Q})$ , where  $V^+(\mathbf{Q})$  is the potential energy surface with the active electron removed (and without the external field), and  $G_0(t, t')$  is just another Green's function, given instead by

$$\left[ i\partial_t - T_N^{\text{vib}} - V^+(\mathbf{Q}) - \frac{\mathbf{p}^2}{2} - \mathbf{F}(t) \cdot \mathbf{r} \right] G_0(t, t') = \delta(t - t'). \quad (3.13)$$

The advantage of rewriting the propagator in the form of Eq. (3.12) is that we obtain a perturbation expansion, in  $\Delta V$ , of the original Green's function

$$G(t, t') = G_0(t, t') + \sum_{n=1}^{\infty} \int_{t'}^t dt_1 \int_{t'}^{t_1} dt_2 \dots \int_{t'}^{t_{n-1}} dt_n G_0(t, t_1) \Delta V G_0(t_1, t_2) \dots \Delta V G_0(t_n, t'). \quad (3.14)$$

If we cut off the series at the  $n$ th term, we refer to it as the  $n$ th order *strong-field approximation* (SFA). It is readily verified by direct calculation that a solution of Eq. (3.13) is given by

$$G_0(t, t') = -i\theta(t - t') \sum_{\nu} \int d\mathbf{k} |\psi_{\mathbf{k}\chi_{\nu}}(t)\rangle \langle \psi_{\mathbf{k}\chi_{\nu}}(t')|, \quad (3.15)$$

if  $\{|\psi_{\mathbf{k}\chi_{\nu}}(t)\rangle\}$  is a complete set of states satisfying

$$\left[ i\partial_t - T_N^{\text{vib}} - V^+(\mathbf{Q}) - \frac{\mathbf{p}^2}{2} - \mathbf{F}(t) \cdot \mathbf{r} \right] |\psi_{\mathbf{k}\chi_{\nu}}(t)\rangle = 0. \quad (3.16)$$

The solution of Eq. (3.16) separates into an electronic and a vibrational part, i.e.,  $|\psi_{\mathbf{k}\chi_{\nu}}(t)\rangle = |\psi_{\mathbf{k}}(t)\rangle \otimes |\chi_{\nu}(t)\rangle$ , with  $|\psi_{\mathbf{k}}(t)\rangle$  a continuum state describing the electron in the laser field, without any Coulomb potential, and  $|\chi_{\nu}(t)\rangle$  is a vibrational eigenstate of the molecular ion with energy  $E_{\nu}$ . The state  $|\psi_{\mathbf{k}}(t)\rangle$  is known as a *Volkov wave function*, and in the position basis it takes the form

$$\psi_{\mathbf{k}}(\mathbf{r}, t) = (2\pi)^{-3/2} \exp \left\{ i \left[ (\mathbf{k} + \mathbf{A}(t)) \cdot \mathbf{r} - \int_{t_0}^t dt' \frac{(\mathbf{k} + \mathbf{A}(t'))^2}{2} \right] \right\}, \quad (3.17)$$

with  $\mathbf{A}(t) = -\int dt \mathbf{F}(t)$  the vector potential corresponding to the electric field of the harmonic-generating laser. We shall proceed using the zeroth-order SFA, that is to say, we replace  $G(t, t')$  in Eq. (3.10) by  $G_0(t, t')$  to obtain  $|\psi_{\lambda\chi_0}(t)\rangle$ .<sup>4</sup> Furthermore, the fact

<sup>4</sup>In doing this, we throw away terms corresponding to continuum-continuum transitions via the potential  $\Delta V$ . These terms represent rescattering of the active electron and, in addition, accounts for the interaction of the ion with the electric field.

that the nuclear motion is slow compared to the electronic motion implies that the electronic wave function will vary only slowly with respect to the nuclear coordinates. We therefore evaluate the initial electronic wave function at the nuclear equilibrium distance,  $\bar{\psi}_\lambda(\mathbf{R}; \mathbf{r}) = \psi_\lambda(\mathbf{R}; \mathbf{Q}_0; \mathbf{r})$ . We may then insert the resulting  $|\bar{\psi}_\lambda \chi_0(t)\rangle$  into Eq. (3.5) and, including only bound-continuum transitions, we obtain

$$\langle \mathbf{d}_\lambda(\mathbf{R}, t) \rangle \simeq i \int_{t_0}^t dt' C(t-t') \int d\mathbf{k} \mathbf{d}_e^*(\mathbf{k} + \mathbf{A}(t)) \exp[-iS_L(\mathbf{k}, t, t')] [\mathbf{F}(t') \cdot \mathbf{d}_e(\mathbf{k} + \mathbf{A}(t'))] + \text{complex conjugate}, \quad (3.18)$$

with

$$\mathbf{d}_e(\mathbf{k}) = \frac{1}{(2\pi)^{3/2}} \int d\mathbf{r} e^{-i\mathbf{k}\cdot\mathbf{r}} \mathbf{r} \bar{\psi}_\lambda(\mathbf{R}; \mathbf{r}), \quad (3.19)$$

$$S_L(\mathbf{k}, t, t') = \int_{t'}^t dt'' \left[ \frac{(\mathbf{k} + \mathbf{A}(t''))^2}{2} - E_0 \right], \quad (3.20)$$

$$C(t-t') = \sum_\nu \left| \int d\mathbf{Q} \chi_\nu^*(\mathbf{Q}) \chi_0(\mathbf{Q}) \right|^2 e^{-iE_\nu(t-t')}. \quad (3.21)$$

The dipole in Eq. (3.18) is usually presented as the result of a three-step process [21]: The electron ionizes to the continuum at time  $t'$  with probability amplitude  $\mathbf{F}(t') \cdot \mathbf{d}_e(\mathbf{k} + \mathbf{A}(t'))$ . It then propagates in the field until time  $t$  acquiring a phase factor  $S_L(\mathbf{k}, t, t')$  and recombines with a probability amplitude  $\mathbf{d}_e^*(\mathbf{k} + \mathbf{A}(t))$  weighted with a factor  $C(t-t')$  due to vibrations of the nuclei. Note that the vibrational factor is proportional to the sum of *Franck-Condon (FC) factors*  $|\int d\mathbf{Q} \chi_\nu(\mathbf{Q})^* \chi_0(\mathbf{Q})|^2$ .

### 3.4.3 The effect of vibration

An interpretation of the vibrational factor (3.21) has been given by Lein [22]: As the molecule is ionized the ground vibrational state of the molecule suddenly experiences the potential energy surface corresponding to the ion, and thus is no longer an eigenstate. Instead, it should be treated as a superposition of the vibrational eigenstates of the molecular ion, and the amplitude of each term is merely the FC amplitude, viz., the overlap of the initial vibrational state with the ion vibrational eigenstate. As a result, the ionization gives rise to a vibrational wave packet  $\chi(\mathbf{Q}, \tau) = \sum_\nu [\int d\mathbf{Q}' \chi_\nu^*(\mathbf{Q}') \chi_0(\mathbf{Q}')] \chi_\nu(\mathbf{Q}) e^{-iE_\nu \tau}$ . The recombination probability amplitude of the electron at time  $t$  will then be proportional to the overlap of the vibrational wave packet with the initial ground vibrational state of the molecule. The principle is illustrated in Fig. 3.3a. Mathematically, the interpretation is verified by rewriting the vibrational factor in terms of the autocorrelation function of the wavepacket<sup>5</sup>

$$C(t-t') = \int d\mathbf{Q} \chi^*(\mathbf{Q}, 0) \chi(\mathbf{Q}, t-t'). \quad (3.22)$$

The period of an optical cycle of the laser field yields an estimate of the characteristic time difference  $t-t'$  entering Eq. (3.22), since the electron is typically launched into the

<sup>5</sup>In Dirac notation this follows easily from Eq. (3.21) by using the closure of the ion vibrational states:  $C(t-t') = \sum_\nu \langle \chi_0 | \chi_\nu \rangle \langle \chi_\nu | \chi_0 \rangle e^{-iE_\nu(t-t')} = \sum_\nu \langle \chi_0 | (\sum_{\nu'} |\chi_{\nu'}\rangle \langle \chi_{\nu'}|) | \chi_\nu \rangle \langle \chi_\nu | \chi_0 \rangle e^{-iE_\nu(t-t')} = \int d\mathbf{Q} [\sum_{\nu'} \langle \chi_{\nu'} | \chi_0 \rangle \chi_{\nu'}(\mathbf{Q})]^* [\sum_\nu \langle \chi_\nu | \chi_0 \rangle \chi_\nu(\mathbf{Q})] e^{-iE_\nu(t-t')}$ .

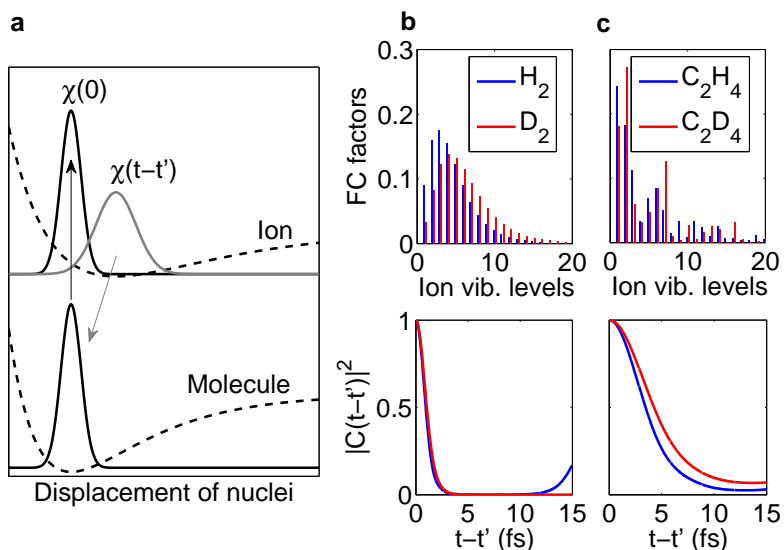


**Figure 3.3 | The effect of nuclear vibration.** **a**, The transition to the molecular ion energy surface launches the wave packet  $\chi$ , and its autocorrelation function, i.e., the overlap  $C(t-t')$  of  $\chi(t-t')$  with  $\chi(0)$ , weights the dipole that generates harmonics [see Eq. (3.18)]. **b** and **c**, Franck-Condon factors and the resulting weight probabilities  $|C(t-t')|^2$  for the  $H_2$  [23] and  $C_2H_4$  [24] molecules along with isotopes. Note how the autocorrelation functions of the heavier isotopes change more slowly.

continuum within one half of an optical cycle and is driven back to recombine with the molecular ion within the other half. For an 800 nm harmonic-generating laser the time difference is of the order femtosecond, and we infer that the harmonic spectrum contains information about the vibrational motion on a femtosecond time scale. On the other hand, vibration will only be of importance if the correlation function changes appreciably within a few femtoseconds, which amounts to saying that the nuclei must be light so that a broad range of ionic vibrational levels, separated by only small energies, are populated. As FC factors and vibrational energies are available for a vast number of molecules, the influence of vibration is readily studied. Figure 3.3b-c illustrates some cases in which vibration might affect the harmonic spectrum appreciably.

For the remainder of this report we shall ignore vibration, which in Eq. (3.18) amounts to replacing the sum over FC factors by unity and  $E_\nu - E_0$  by  $I_P$ , the experimental adiabatic ionization potential, which is available from [25]. Instead, we refer to Ref. [2] for calculations that include vibration.

### 3.4.4 Calculating the dipole

Ignoring vibration, all we need is the electronic wave function in order to evaluate the dipole in Eq. (3.18). The field-free initial state of the active electron, the HOMO wave function, is conveniently expressed in an expansion on spherical harmonics in the MF frame

$$\bar{\psi}_\lambda^{\text{MF}}(\mathbf{r}) = \sum_{l,m} F_{l,m}^\lambda(r) Y_l^m(\hat{\mathbf{r}}). \quad (3.23)$$

Asymptotically this expression follows the Coulomb form

$$\bar{\psi}_\lambda^{\text{MF}}(\mathbf{r}) \sim \sum_{l,m} C_{l,m}^\lambda r^{1/\kappa-1} \exp(-\kappa r) Y_l^m(\hat{\mathbf{r}}) \quad (3.24)$$

with  $\kappa = \sqrt{2I_P}$  and where the  $C_{l,m}^\lambda$ 's are constants. We wish to carry out calculations in the LF frame, and for a molecule of arbitrary orientation this will not coincide with the MF frame. Hence, we rotate the MF wave function by application of the rotation operator

$$\bar{\psi}_\lambda(\mathcal{R}; \mathbf{r}) = \hat{D}(\mathcal{R}) \bar{\psi}_\lambda^{\text{MF}}(\mathbf{r}). \quad (3.25)$$

Note that the effect of  $\hat{D}(\mathcal{R})$  is readily evaluated in the spherical harmonic basis used in Eqs. (3.23) and (3.24) [10].

With the initial electronic wave function at hand there are various ways to evaluate the electronic dipole of Eq. (3.18). By far the most popular approach is that of Lewenstein [21]. Instead, we will assume that the harmonic laser pulse contains several cycles so that the field can be considered as monochromatic.<sup>6</sup> We can then describe the laser field by the vector potential  $\mathbf{A}(t) = \mathbf{A}_0 \cos(\omega t)$ , and the photon picture from Sec. 3.3 on page 16 is beautifully linked with the three-step model provided below Eq. (3.18): The HOMO electron is first transferred to the continuum via *above threshold ionization* (ATI), i.e., by absorbing a number of photons from the driving laser. The electron then propagates in the laser-dressed continuum and is eventually, due to the periodicity of the laser field, driven back to a recombination with the molecule, where it returns to the HOMO by emission of a harmonic photon. Within this model the complex amplitude for the emission of harmonics polarized along the unit vector  $\mathbf{e}$  with frequency  $\omega_{\text{HHG}}^N = N\omega$  ( $N$  integer), denoted the  $N$ th harmonics or harmonics of order  $N$ , is given by<sup>7</sup>

$$\begin{aligned} A_e^\lambda(\omega_{\text{HHG}}^N, \mathcal{R}) &= (N\omega)^2 \sum_{l_2, l_1} \sum_{m'_2, m'_1} \sum_{m_2, m_1} D_{m'_2, m_2}^{l_2*}(\mathcal{R}) D_{m'_1, m_1}^{l_1}(\mathcal{R}) \\ &\times C_{l_1, m_1}^\lambda \sum_k \sum_{C(k)} B_{l_2, m'_2, m_2}^{\lambda, N, k, e}(C(k)) A_{l_1, m'_1}^k(C(k)). \end{aligned} \quad (3.26)$$

Here  $D_{m'_i, m_i}^l(\mathcal{R})$  with  $i = 1, 2$  is the Wigner rotation function [10], while

$$\begin{aligned} C_{l_1, m_1}^\lambda A_{l_1, m'_1}^k(C(k)) &= -C_{l_1, m_1}^\lambda \frac{1}{T} \Gamma \left( 1 + \frac{1/\kappa}{2} \right) 2^{\frac{1/\kappa}{2}} \kappa^{1/\kappa} (\pm 1)^{l_1} \frac{\exp[iS(t'_{C(k)})]}{\sqrt{[-iS''(t'_{C(k)})]^{1+1/\kappa}}} \\ &\times Y_{l_1}^{m'_1}(\hat{\mathbf{q}}') \Big|_{\mathbf{q}' = \mathbf{K}_k + \mathbf{A}(t'_{C(k)})} \end{aligned} \quad (3.27)$$

and

$$\begin{aligned} B_{l_2, m'_2, m_2}^{\lambda, N, k, e}(C(k)) &= i \frac{(2\pi)^2}{T} \int_0^T dt \frac{\exp[i(N\omega t - S(t))]}{L_0(t, t'_{C(k)})} (\mathbf{e} \cdot \nabla_{\mathbf{q}}) \\ &\times \left[ \tilde{F}_{l_2, m_2}^\lambda(q) Y_{l_2}^{m'_2}(\hat{\mathbf{q}}) \right]^* \Big|_{\mathbf{q} = \mathbf{K}_k + \mathbf{A}(t)}, \end{aligned} \quad (3.28)$$

<sup>6</sup>If the field consists of, say, ten laser cycles it will still be short on the rotational time scale, so that the rotational degrees of freedom may be considered as frozen.

<sup>7</sup>Note the factor of  $(N\omega)^2$ , which comes about, because we obtain the dipole acceleration directly from the Fourier transform of the dipole. This can only be done if the dipole relaxes to its initial value after the pulse [15]. We thus assume that the electron remains bound after the laser pulse has gone or that the electron is isotropically ejected from the molecule.

along with their Wigner rotation functions, are interpreted as ATI and propagation-recombination amplitudes, respectively, of a HOMO electron having absorbed  $k$  photons during the ATI-step. In Eqs. (3.27) and (3.28)  $\mathbf{q}$  and  $\mathbf{q}'$  are electron momenta and

$$S(t) = k\omega t + \mathbf{K}_k \cdot \frac{\mathbf{A}_0}{\omega} \sin(\omega t) + \frac{U_p}{2\omega} \sin(2\omega t). \quad (3.29)$$

The index  $C(k)$  in Eqs. (3.26)-(3.28) denotes saddle-points. For each  $k$  the saddle-points  $t'_{C(k)}$  are defined by the condition  $S'(t'_{C(k)}) = 0$ , and we use the ones with  $0 \leq \text{Re}(t'_{C(k)}) < T$  along with  $\text{Im}(t'_{C(k)}) > 0$ . The factors  $(\pm 1)^{l_1}$  in Eq. (3.27) correspond to the limits  $\pm i\kappa$  of the size  $q'$  of the electron momentum at the saddle-points. The factor  $1/L_0(t, t'_{C(k)}) = \sigma\alpha_0(\sin \omega t'_{C(k)} - \sin \omega t)$  in Eq. (3.28), with  $\sigma = \pm 1$  to assure  $\text{Re}(L_0) > 0$ , describes the decrease of the amplitude of the electron wave as it propagates in the field-dressed continuum. Also,  $\mathbf{K}_k$  is the part of the continuum electron momentum arising from absorption of  $k$  laser photons during ATI, thus  $K_k = \sqrt{2(k\omega - I_p - U_p)}$  with  $U_p = A_0^2/4$  the ponderomotive potential and  $\mathbf{e}_{\mathbf{K}_k} = \sigma \mathbf{e}_{\mathbf{A}_0}$ . Finally, in Eq. (3.28) the function  $\tilde{F}_{l_2, m_2}^\lambda(q)$  is the radial part of the momentum space HOMO wave function, obtained by taking the Fourier transform of Eq. (3.25) (see Refs. [2, 26] for further details).

## 3.5 Results

In this section we use the model developed above to study the effects of molecular orientation, orbital symmetry and degeneracy on the harmonic spectrum. All of the HOMO wave functions have been determined from a Hartree-Fock method using the computational chemistry software GAMESS [27].

### 3.5.1 High-order harmonic generation from alkanes

We begin by considering HHG from alkanes aiming at isolating and illustrating clearly the effects of symmetry, degenerate orbitals and orientation. We calculate the signal of harmonics polarized along the linearly polarized 800 nm,  $1.8 \times 10^{14}$  W/cm<sup>2</sup> driving laser and choosing the LF  $Z$  axis along the polarization direction the results become independent of  $\phi$ , the rotation of the molecule around the polarization vector. We shall assume that the molecules are either unaligned or have been one- or three-dimensionally oriented. The orientational distributions corresponding to random, one-dimensional and three-dimensional orientation are as follows

$$G_{t_d}^{\text{Unaligned}} = \frac{1}{8\pi^2}, \quad (3.30)$$

$$G_{t_d}^{1\text{D}}(\theta', \chi') = \frac{1}{4\pi^2} \frac{\delta(\theta' - \theta)}{\sin \theta'}, \quad (3.31)$$

$$G_{t_d}^{3\text{D}}(\theta', \chi') = \frac{1}{2\pi} \frac{\delta(\theta' - \theta)}{\sin \theta'} \delta(\chi' - \chi). \quad (3.32)$$

Here the MF  $z$  axis is oriented at an angle  $\theta$  with respect to the LF  $Z$  axis in the cases of one- and three-dimensional orientation and the molecule is rotated an angle  $\chi$  around the MF  $z$  axis in the case of three-dimensional orientation.

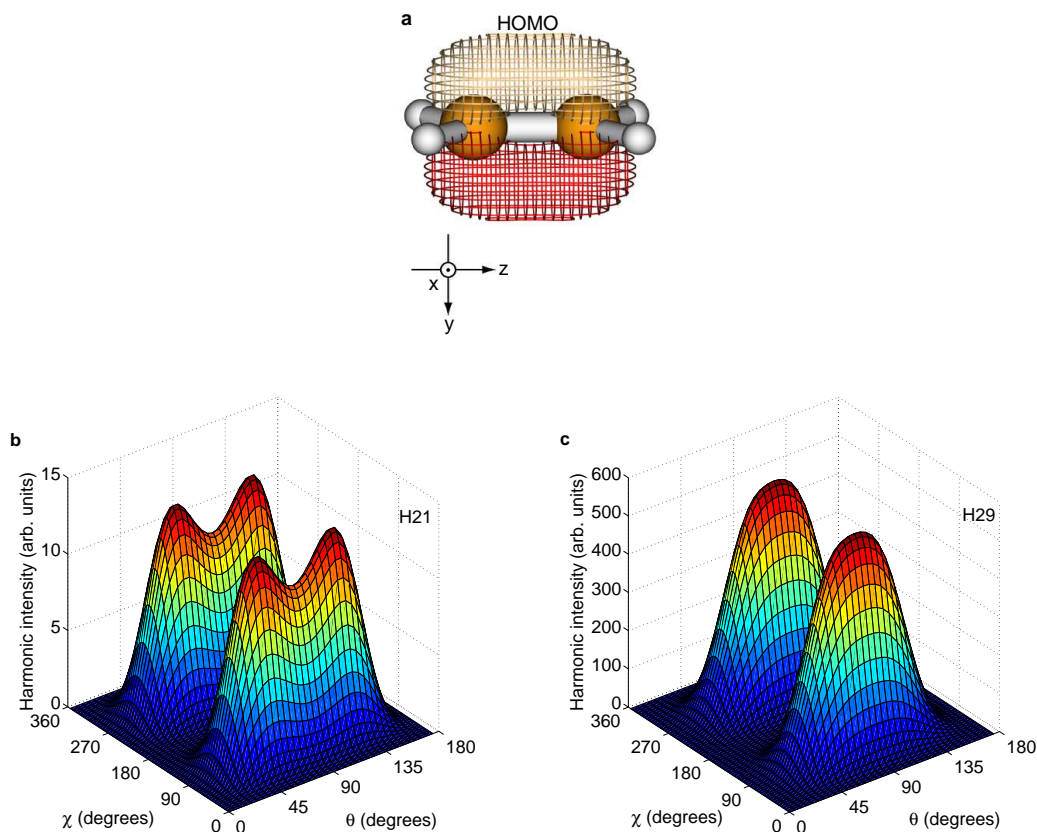


**Figure 3.4 | Effect of orbital symmetry in HHG.** Example with ethylene ( $C_2H_4$ ). **a**, The geometry of ethylene ( $C_2H_4$ ) along with an isocontour for the HOMO. We use the color red to indicate a negative sign of the HOMO wave function and brownish to indicate a positive sign. Directions of the MF axes are shown, but we use the center of mass as the origin of the MF coordinate system. **b** and **c**, The dependencies of the 21st (H21) and 29th (H29) harmonics on orientation as given by Euler angles  $\theta$  and  $\chi$  (defined on page 15). The results are for an 800 nm harmonic-generating pulse of intensity  $1.8 \times 10^{14} \text{ W/cm}^2$ .

### Ethylene: Effect of orbital symmetry

We first present results on the HHG from ethylene ( $C_2H_4$ ). This molecule has a non-degenerate HOMO which makes the influence of the HOMO on the harmonic signal relatively transparent. Figure 3.4 shows representative results of the investigation of HHG from  $C_2H_4$  that has been fixed in both  $\theta$ - and  $\chi$ -angles corresponding to the three-dimensional orientation given by Eq. (3.32). In order to understand the results, we also show the HOMO of ethylene in the figure. In the model used to simulate HHG an electron has to escape along the laser polarization axis [cf. Eq. (3.27)]. This is impossible, if the polarization axis lies along the nodal plane, which is the reason for the vanishing harmonic signal, when either  $\theta = 0^\circ$  ( $180^\circ$ ) or  $\chi = 0^\circ$  ( $180^\circ$ ,  $360^\circ$ ). When the molecule is rotated, the nodal plane is removed from the polarization axis of the laser and the strength of the harmonics increases. As seen from Figs. 3.4b-c the harmonics peak at different values of the Euler angle  $\theta$ . The varying positions of the peaks arise from competing effects of the ionization and propagation-recombination steps making up the HHG process: As the electron escapes along the polarization direction the ionization is maximal when  $\theta$  lies in between  $0^\circ$  and  $90^\circ$ . The propagation-recombination step, however, is optimized when

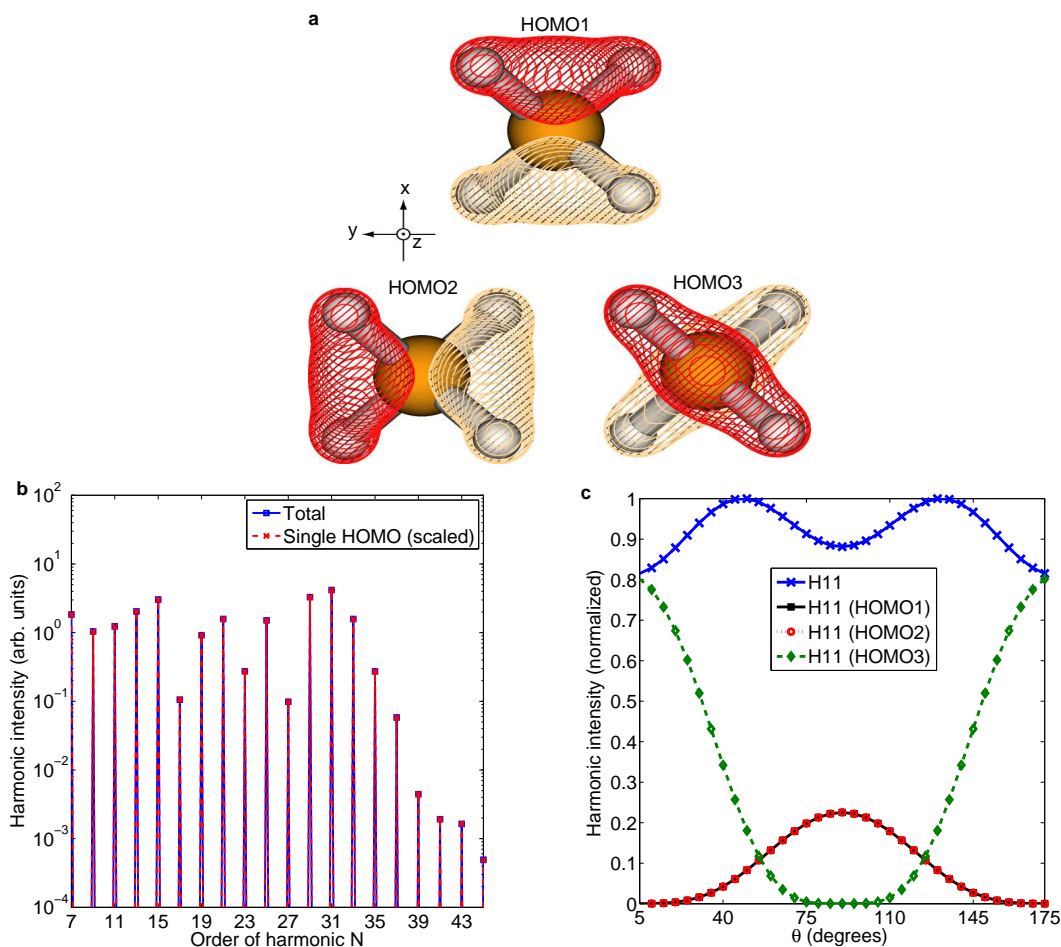


**Figure 3.5 | HHG in the case of degenerate HOMOs.** Example with methane (CH<sub>4</sub>). A laser of wavelength 800 nm and intensity  $1.8 \times 10^{14}$  W/cm<sup>2</sup> drives the HHG. **a**, Isocontours of the three degenerate HOMOs. **b**, The harmonic spectrum of unaligned methane is proportional to the spectrum of a single HOMO. **c**, The  $\theta$ -dependence of the 11th harmonic (H11). We also show the intensity of the single HOMO signals.

$\theta = 90^\circ$ , but the width of the peak depends on the harmonic order. These observations account for the different orientational behavior of the harmonics shown in Fig. 3.4b-c.

We note, in passing, that a set of data as the ones presented in Fig. 3.4b-c for a full range of harmonic energies would, in principle, allow a tomographic reconstruction of the HOMO [28].

### Methane: Interference due to degenerate HOMOs

We now turn to the harmonic yield from the methane molecule (CH<sub>4</sub>). Methane has three degenerate HOMOs as shown in Fig. 3.5a, and we can use this molecule to demonstrate the effect discussed below Eq. (3.7), i.e., the absence of interference effects from unaligned molecules, when the degenerate HOMOs differ only by a rotation. To this end we have compared the total harmonic yield with the yield from a single HOMO when the orientational distribution is as given by Eq. (3.30) and confirmed that the results agree except from an overall factor. This is illustrated in Fig 3.5b.

Next, we have carried out calculations on HHG from methane that has been one-dimensionally oriented with the MF  $z$  axis at some fixed angle  $\theta$  relative to the polarization direction. The orientational distribution used is given by Eq. (3.31). We do not show the harmonic spectrum in this case, since it does not differ much in structure from the one in Fig. 3.5b. This is probably due to the fact that methane is small and compact, which makes it spherical-like after  $\chi$ -averaging. Consequently, no structure is revealed by the electrons, not even the most energetic, and the harmonics exhibit the same overall  $\theta$ -dependence. In Fig. 3.5c we show this typical angular dependence of the harmonics. Here the upper curve shows the signal when the coherence between the individual HOMOs is correctly accounted for [cf. Eq. (3.7)]. The other curves in the figure show the unphysical signals from each HOMO. Clearly, this figure illustrates that there is a strong interference between the single HOMO dipoles in the angle resolved signal. We may understand the single HOMO signals in Fig. 3.5c from the structure of the HOMOs: First, we explain the dips. The vanishing signals of HOMO1 and HOMO2 at  $\theta = 0^\circ$  are explained by the fact that in this case the polarization vector points along the MF  $z$  axis, hence coinciding with the nodal planes of these HOMOs, as seen from Fig. 3.5a. Furthermore, the electron causing HHG must escape along the polarization axis according to Eq. (3.27), and we conclude that these two HOMOs cannot generate harmonics for  $\theta = 0^\circ$ . At  $\theta = 90^\circ$  the polarization axis is directed into the MF  $xy$ -plane which is also the nodal plane of HOMO3 (see Fig. 3.5a) and consequently HHG from HOMO3 is excluded. Second, we remark that the single HOMO-yield at a given value of  $\theta$  is obtained by averaging amplitudes from all degrees of rotation around the MF  $z$  axis [cf. Eqs. (3.7) and (3.31)]. It is therefore obvious that the results of HOMO1 and HOMO2 must be identical.

### Propane: Effect of orientation

In the following we consider propane ( $C_3H_8$ ). Figure 3.6 on the facing page shows the HOMO of propane along with the harmonic signal in unaligned and one-dimensionally oriented scenarios corresponding to orientational distributions from Eqs. (3.30) and (3.31). The dependence of the HHG spectrum on orientation amounts to more than just a scaling, e.g., the 19th harmonic is at the same or a lower intensity compared to the neighboring odd harmonics depending on the orientation of the propane molecule. We ascribe this to the fact that propane is a rather extended and open-structured molecule. In general, when the MF  $z$  axis is close to the LF  $Z$  axis the HHG is suppressed, because the almost vanishing wave function along the polarization direction (see Fig. 3.6b) makes the ATI amplitudes in Eq. (3.26) small. Notice also that the even harmonics disappear at an orientation of  $90^\circ$ . In the photon picture, this is understood from the fact that every photon absorption at this orientation changes the projection of the electronic orbital angular momentum on the  $z$  axis with  $\pm\hbar$ , and as the MF HOMO wave function contains only odd  $m$  components an odd number of photon absorptions is required to return to the HOMO in the emission step (cf. Fig. 3.2 on page 17).

We remark that harmonics of order 15 to 27 are suppressed for  $\theta = 90^\circ$ , which means that alignment is a tool for promoting the harmonics close to and above the semi-classical cutoff energy at  $I_p + 3.17U_p \simeq 29 \times \hbar\omega$ . These harmonics are known to be well phase-synchronized in the case of diatomic molecules, and this may also hold true in the case of propane. Furthermore, phase-synchronized harmonics are synchronically emitted and the superposition of such harmonics constitutes the basis for the generation of attosecond pulses.

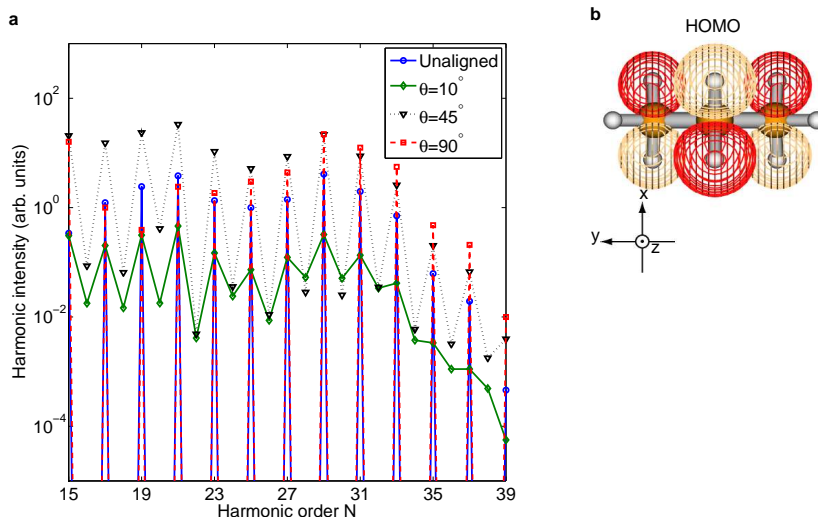


**Figure 3.6 | Selecting harmonics by orientation.** The open and extended structure of propane ( $C_3H_8$ ) leads to a harmonic spectrum with a complicated orientational dependence as illustrated in **a**. In particular, harmonics near the semi-classical cutoff ( $N = 29$ ) are promoted at  $\theta = 90^\circ$ . **b**, Isocontour of the HOMO.

### 3.5.2 Generation of even harmonics from the CO molecule

For the HHG experiments conducted so far the orientational distributions of molecules have been inversion symmetric with respect to the polarization axis of the harmonic-generating laser, and therefore even harmonics have not been observed. Here we propose an experimental setup with a gas of CO molecules (in the  $\Sigma$  electronic ground state) that would lead to even harmonics. To accomplish this we have to orient the molecules, and this is done using two electric fields of the same linear polarization direction, which specifies the LF  $Z$  axis. The electric field, breaking the inversion symmetry, is that of a half cycle pulse (HCP) [29],  $F_{\text{orient}}(t) = F_0 \cos^2(\pi t/t_p)$ , with amplitude  $F_0 = 870$  kV/cm and pulse duration  $t_p = 0.5$  ps. It is followed 4.14 ps later by an alignment pulse with FWHM of 0.5 ps and intensity  $5 \times 10^{12}$  W/cm<sup>2</sup> (see page 8 for details on the alignment envelope function). Using an initial rotational temperature of 5 K, we obtain the time-dependent orientational distribution shown in Fig. 3.7a. We observe a clear asymmetry about  $90^\circ$  at time  $t_d = 8.1$  ps after the peak of the HCP. At this instant we should be able to drive even harmonics, as confirmed in panel b showing the emitted high-order harmonics generated by an 800 nm,  $2 \times 10^{14}$  W/cm<sup>2</sup> laser field with both harmonics and the driving field of the same polarization direction as the pump pulses.

## 3.6 Discussion of gauges and forms

To end this chapter we consider an issue of purely theoretical interest. Our treatment of HHG began with the length gauge time-dependent Schrödinger equation (3.1) in Sec. 3.1. By introducing a unitary transformation the interaction of the molecule with the laser field may be recast into the form  $V'_{\text{HHG}}(t) = \sum_n \mathbf{A}(t) \cdot \mathbf{p}_n + \mathbf{A}^2(t)/2$ , which is known as the *velocity gauge* representation, since it couples the vector potential to the velocity operator. A third representation of the interaction, denoted *acceleration gauge* or

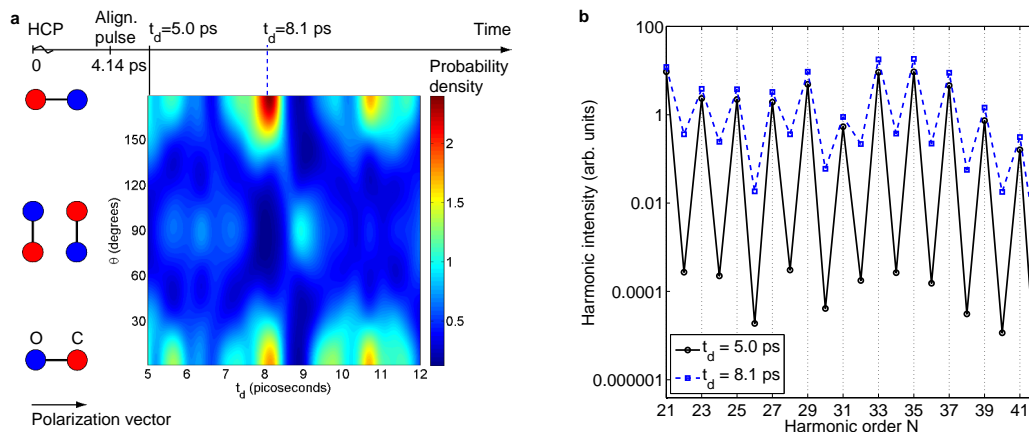


**Figure 3.7 | Generation of even harmonics from the CO molecule.** **a**, Orientational distribution,  $G_{t_d}$ , after orientation by a half cycle pulse (HCP) and an alignment pulse. **b**, HHG yield from CO at delay  $t_d$  with respect to the HCP using an 800 nm driving pulse of intensity  $2 \times 10^{14}$  W/cm<sup>2</sup>. Even harmonics are observed for  $t_d = 8.1$  ps, and we also show the generated harmonics for  $t_d = 5$  ps as a reference. [Note that by choosing the LF  $Z$  axis along the linear polarization axis (of all pulses) the problem becomes independent of the  $\chi$  and  $\phi$  Euler angles.]

*Kramers-Henneberger frame* can be obtained by shifting to a moving frame centered at the position of a free electron subject to the oscillations of the field. Observables have the same value independent of the gauge chosen as long as the time-dependent Schrödinger equation is solved exactly.

The range of options for calculating a harmonic spectrum is even wider: The dipole acceleration appearing in Eq. (3.2) needs not to be obtained from the so-called *length form*, where the second time derivative of the dipole is calculated directly. By exploiting that  $|\Psi(t)\rangle$  satisfies Eq. (3.1), along with the commutation relations of the position and momentum operators with the length gauge Hamiltonian, one can readily derive the equivalent *velocity form*,  $d^2\langle\mathbf{d}(t)\rangle/dt^2 = d\langle\Psi(t)| - \sum_n \mathbf{p}_n |\Psi(t)\rangle/dt$  and the *acceleration form*,  $d^2\langle\mathbf{d}(t)\rangle/dt^2 = \langle\Psi(t)| \sum_n [\nabla_{\mathbf{r}_n} V_C + \mathbf{F}(t)] |\Psi(t)\rangle$ .

Altogether, we are then left with nine ways to calculate the HHG spectrum (one for each combination of gauge and form). Now, if this was the end of the story one should choose the gauge and form that facilitate calculations mostly. As soon as the SFA is employed, however, a problem arises, because we are no longer dealing with an exact solution of the Schrödinger equation. This fact invalidates the equivalence of gauges and of forms. Consequently, we get different HHG spectra with different choices of gauge and form, and while some combinations are optimal in some cases, other situations call for a different choice of gauge and form [30, 31].

---

## Conclusion and outlook

In conclusion this progress report has treated several aspects of alignment and high-order harmonic generation from molecules. In Chapter 2 we developed a semi-classical model that accounted for the observations of a pioneering experiment on the control of internal motion of the DFDBrBP molecule using laser induced alignment. With this model at our disposal, we were moreover able to demonstrate how future experiments may succeed in de-racemization. Chapter 3 treated high-order harmonic generation from molecules, and in particular we saw how to take into account partly or completely frozen degrees of freedom. The effect of vibration was briefly discussed and next the effects of molecular symmetry, degeneracy and orientation in HHG was demonstrated by model calculations on alkanes and the CO molecule.

The results presented in this report give rise to a number of new challenges. In the nearest future the work on DFDBrBP and similar molecules will continue. The current calculations might be improved by maintaining the coupling of  $\Phi$  and  $\phi_d$  [cf. Eqs. (2.8) and (2.9)]. Also, we considered only the torsion of the two rigid rings. It would be interesting to study the interaction of other normal modes with the lasers by deriving a field-free rigid bender Hamiltonian along the lines of Ref. [32]. In relation to a new series of experiments, an optimization of the de-racemization process would be of relevance. It can readily be carried out with the number of kick pulses and the polarization direction, intensity and duration of each of these pulses as parameters, or, alternatively, an approach based on optimal control theory might be considered. Another evident continuation of the project is to study HHG from biphenyl as a function of the dihedral angle. The ability to control the initial state of internal motion provides an interesting new tool to shape the harmonic spectra. Moreover, it is conceivable that the harmonic spectrum yields useful time-resolved information on the normal modes of the molecule.

All calculations of HHG spectra presented in this report are based on the length gauge and the dipole form. In the light of the discussion provided in Sec. 3.6 on page 27, we need to carry out calculations using different gauges and forms, although we expect the conclusions drawn in Chapter 3 to be fairly model independent. In this context, it would also be attractive to replace the current procedure for evaluation of the dipole with the one of Lewenstein [21], partly because the latter is more common within the research community, and partly because it can be directly applied when the harmonic-generating

pulse consists of only a few cycles.

Going into a different direction, a new mechanism, closely related to HHG, is envisioned by decoupling the ionization step from the subsequent propagation and recombination of the electron. The decoupling can be achieved by using an extreme ultraviolet attosecond pulse to launch the electron into the continuum through single photon ionization at a well defined phase of a synchronized infrared field, which drives the dynamics from that point forward [33]. Alone studying the phase dependence for this process from a simple system, such as the hydrogen atom, will be of interest.

We remarked in Sec. 3.6 that a full HHG calculation in general consists of two steps, viz., the treatment of the single-molecule response to the field and the propagation of the laser field along with the harmonics through the generating medium. Experimenters have pointed out repeatedly that the latter mechanism is important. For example, effects that are predicted without it might disappear. Consequently, an implementation of propagation effects is of some interest. The first thing to do is then to combine Maxwell's equations into the optical wave equation [34]. In the case of HHG, the polarizability has one very important nonlinear term, namely the one, which couples the fundamental frequency field to the high-order harmonics [35] and, knowing the neutral molecular density of the gas, the term can be worked out from the single-molecular dipole described in Chapter 3. To actually solve the propagation equation, it is split into two separate equations that effectively describe the fundamental field and the harmonic field, respectively. Such equations can, e.g., be found in Ref. [36].

Looking a little further into the future, it will be of interest to go beyond the SAE approximation and study the role of electron-electron correlation. The natural approach will be to include two electrons and to use a modified mean-field potential in which a division into inner and outer electrons reduces the dimensionality of the actual problem. A numerical project could be the implementation of HHG in the code for propagation of the time-dependent Schrödinger equation that was developed by Thomas Kim Kjeldsen [37]. With such code, HHG from a molecule of arbitrary orientation with respect to the harmonic-generating laser polarization axis can be studied by ab initio methods.



---

# Bibliography

- [1] V. Kumarappan, L. Holmegaard, C. Martiny, C. B. Madsen, T. K. Kjeldsen, S. S. Viftrup, L. B. Madsen, and H. Stapelfeldt, *Phys. Rev. Lett.* **100**, 093006 (2008).
- [2] C. B. Madsen and L. B. Madsen, *Phys. Rev. A* **74**, 023403 (2006).
- [3] C. B. Madsen, A. S. Mouritzen, T. K. Kjeldsen, and L. B. Madsen, *Phys. Rev. A* **76**, 035401 (2007).
- [4] C. B. Madsen and L. B. Madsen, *Phys. Rev. A* **76**, 043419 (2007).
- [5] H. Stapelfeldt and T. Seideman, *Rev. Mod. Phys.* **75**, 543 (2003).
- [6] B. W. Shore, *The theory of coherent atomic excitation*, vol. I and II (John Wiley, New York, 1990).
- [7] F. Grein, *J. Phys. Chem. A* **106**, 3823 (2002).
- [8] K. Hoki, D. Kröner, and J. Manz, *Chem. Phys.* **267**, 59 (2001).
- [9] J. J. Sakurai, *Modern quantum mechanics* (Addison-Wesley Publishing Company, New York, 1994), revised ed.
- [10] R. N. Zare, *Angular momentum: understanding spatial aspects in chemistry and physics* (John Wiley, New York, 1988).
- [11] S. Ramakrishna and T. Seideman, *Phys. Rev. Lett.* **99**, 103001 (2007).
- [12] R. Noyori, *Angew. Chem. Int. Ed.* **41**, 2008 (2002).
- [13] P. Brumer, E. Frishman, and M. Shapiro, *Phys. Rev. A* **65**, 015401 (2001).
- [14] A. McPherson, G. Gibson, H. Jara, U. Johann, T. S. Luk, I. A. McIntyre, K. Boyer, and C. K. Rhodes, *J. Opt. Soc. Am. B* **4**, 595 (1987).
- [15] K. Burnett, V. C. Reed, J. Cooper, and P. L. Knight, *Phys. Rev. A* **45**, 3347 (1992).
- [16] B. Sundaram and P. W. Milonni, *Phys. Rev. A* **41**, 6571 (1990).

## Bibliography

- [17] T. Kanai, S. Minemoto, and H. Sakai, *Nature (London)* **435**, 470 (2005).
- [18] J. Itatani, D. Zeidler, J. Levesque, M. Spanner, D. M. Villeneuve, and P. B. Corkum, *Phys. Rev. Lett.* **94**, 123902 (2005).
- [19] R. Santra and A. Gordon, *Phys. Rev. Lett.* **96**, 073906 (2006).
- [20] E. U. Condon, *Phys. Rev.* **36**, 1121 (1930).
- [21] M. Lewenstein, P. Balcou, M. Y. Ivanov, A. L’Huillier, and P. B. Corkum, *Phys. Rev. A* **49**, 2117 (1994).
- [22] M. Lein, *Phys. Rev. Lett.* **94**, 053004 (2005).
- [23] G. H. Dunn, *J. Chem. Phys.* **44**, 2592 (1966).
- [24] J. M. Luis, M. Torrent-Sucarrat, M. Solà, D. M. Bishop, and B. Kirtman, *J. Chem. Phys.* **122**, 184104 (2005).
- [25] P. J. Linstrom and W. G. Mallard, eds., *NIST Chemistry WebBook, NIST Standard Reference Database Number 69* (National Institute of Standards and Technology, Gaithersburg MD, 20899 (<http://webbook.nist.gov>), 2005).
- [26] M. Y. Kuchiev and V. N. Ostrovsky, *Phys. Rev. A* **60**, 3111 (1999).
- [27] M. W. Schmidt, K. K. Baldridge, J. A. Boatz, S. T. Elbert, M. S. Gordon, J. H. Jensen, S. Koseki, N. Matsunaga, K. A. Nguyen, S. Su, et al., *J. Comput. Chem.* **14**, 1347 (1993).
- [28] J. Itatani, J. Levesque, D. Zeidler, H. Niikura, H. Pépin, J. C. Kieffer, P. B. Corkum, and D. M. Villeneuve, *Nature (London)* **432**, 867 (2004).
- [29] C. M. Dion, A. Keller, and O. Atabek, *Eur. Phys. J. D* **14**, 249 (2001).
- [30] C. C. Chirilă and M. Lein, *Phys. Rev. A* **73**, 023410 (2006).
- [31] C. C. Chirilă and M. Lein, *J. Mod. Opt.* **54**, 1039 (2007).
- [32] P. Jensen, *J. Mol. Spectrosc.* **128**, 478 (1988).
- [33] J. Mauritsson, P. Johnsson, E. Mansten, M. Swoboda, T. Ruchon, A. L’Huillier, and K. J. Schafer, *Phys. Rev. Lett.* **100**, 073003 (2008).
- [34] R. W. Boyd, *Nonlinear optics* (Academic Press, Boston, 1992).
- [35] A. L’Huillier, K. J. Schafer, and K. C. Kulander, *J. Phys. B* **24**, 3315 (1991).
- [36] V. Tosa, H. T. Kim, I. J. Kim, and C. H. Nam, *Phys. Rev. A* **71**, 063807 (2005).
- [37] T. K. Kjeldsen, PhD Thesis, Department of Physics and Astronomy University of Århus (2007).